UNIVERSITAT POLITÈCNICA DE CATALUNYA
BARCELONATECH
Escola d'Enginyeria de Telecomunicació
i Aeroespacial de Castelldefels

TREBALL DE FI DE GRAU

TFG TITLE: Active flow control on cambered airfoils at ultralow Reynolds using synthetic jet

DEGREE: Grau en Enginyeria d'Aeronavegació

AUTHORS: Pau Valdepeñas Pujol

ADVISOR: Fernando Pablo Mellibovsky Elstein

DATE: September 15, 2017

Títol: Control de flux actiu en perfils alar curvats a Reynolds baixos utilitzant sintètic jet

Autors: Pau Valdepeñas Pujol

Director: Fernando Pablo Mellibovsky Elstein

Data: 15 de setembre de 2017

Resum

Els mètodes de control de flux actiu han estat àmpliament estudiats durant més d'una dècada per millorar l'eficiència alar. Aquest estudi està centrat en el control anomenat sintètic jet, el seu èxit com a dispositiu de control de flux actiu ha estat àmpliament recercat per diversos autors. Com es pot observar, la tecnologia del sintètic jet proporciona bons resultats en la reconexiò de la capa límit i, per tant, una millora en les forces aerodinàmiques que actuen sobre l'ala. A més, és un sistema genèric que es pot implementar en diversos tipus de aeronaus com ara desde vehicles aeris no tripulats fins a avions comercials. L'efectivitat en la mitigació de la separació de la capa límit depèn d'una sèrie de paràmetres relacionats tant amb el propi flux com el sistema de control, com ara: la freqüència i l'amplitud de l'excitació, la distribució de l'excitació, el diàmetre de sortida i la forma de la cavitat. Com podem observar aquest sistema consta de diversos graus de llibertat. Per aquest motiu s'han de realitzar múltiples simulacions per tal d'avaluar la millor configuració per aconseguir la màxima eficiència en el perfil alar. La coneguda excitació del jet sintètic és el flux de massa net que combina tant l'expulsió com la succió periòdicament. En aquest estudi, també avaluem altres tipus d'excitació que impliquen una aportació i disminució d'energia en el sistema que hem caracteritzat amb el coeficient de moment. L'objectiu és fer una avaluació detenida d'aquest equilibri existent entre el rendiment aerodinàmic i el coeficient de moment. Finalment, s'extreuen conclusions per tal d'avaluar la millor configuració del sintètic jet per proporciona resultats complets en què el perfils alars milloren la seva aerodinàmica. Per extreure adequadament conclusions, passem per un procés complet i complex que comença amb la discretització genèrica de la malla adaptada pel sintètic jet que utilitzem per resoldre les equacions de Navier-Stokes, seguidament, realitzem les conversions adequades per simular amb la infraestructura d'elements espectrals Nektar ++ i, finalment, l'extracció detallada de resultats. A més a més, en aquest estudi aportem una extenció pràctica amb la fotogrametria de l'ala d'un vehicle aèri no tripulat (UAV Skywalker x6) que utilitzem per a realitzar les corresponents simulacions.

Title : Active flow control on cambered airfoils at ultralow Reynolds using synthetic jet

Authors: Pau Valdepeñas Pujol

Advisor: Fernando Pablo Mellibovsky Elstein

Date: September 15, 2017

Overview

Active flow control methods have been widely studied for more than a decade in order to improve the airfoil's efficiency. This study is focused on fluidic actuation (the addition or subtraction of momentum to/from the boundary layer by blowing and/or sucking fluid). A synthetic jet is a very particular type of fluidic actuation that involves periodic blowing and suction with zero-net-mass-flow over a the full period. Its success as an active flow control device has been extensively reported by several authors. As it can be seen synthetic jet technology provides good results on boundary layer reattachment and therefore, an improvement on the airfoil's efficiency. What is more, is a generic system that can be widespread on multiple types of airfoils such as unmanned aerial vehicles and conventional airplanes airfoils. The effectiveness of control in mitigating boundary separation depends on a number of parameters related both to the flow itself and the control input such as: frequency and amplitude of the excitation, the excitation shape, exit diameter and cavity shape. Since the synthetic jet system has several degrees of freedom and the flux is unpredictable, multiple simulations have to be done in order to assess the best configuration to achieve the maximum airfoil's efficiency. The well-known excitation of the synthetic jet is the zero-net-mass-flow that combines both expulsion and suction periodically. In this study, we also evaluate other types of excitations that imply more or less energy into the system that is characterized with the momentum coefficient. The goal is to assess thoroughly this existent trade-off between the aerodynamics performance and the momentum coefficient. And finally, extract deep conclusions and assess the best synthetic jet configuration where the aerodynamics performances are improved with a low momentum coefficient.. To extract suitably conclusions we pass through a thorough and intricate process that starts with the adapted and generic discretized surface for the synthetic jet that we use to solve the Navier-Stokes equations, then the appropriate conversions to simulate with spectral element framework Nektar++ and finally the detailed extraction of results. Moreover, we adopt to this study a practical approach with an unmanned aerial vehicle (UAV Skywalker x6) airfoil's photogrammetry that we use to simulate.

CONTENTS

LIST OF FIGURES

LIST OF TABLES

INTRODUCTION

Conventional airfoil profiles typically experience severe aerodynamic performances degradation when operated at large angles of attack. Large angles of attack are needed for the crucial operations of take off and landing where high lift and low drag are needed. This degradation of aerodynamic performance is due to the fact that laminar boundary layer separation occurs near the leading edge. If this separation occurs so close to the leading edge, much of the potential part of the airfoil is wasted. In order to optimize the airfoil performances active flow controls has been widely studied for more than a decade.

Active flow control are methods to improve the airfoil's efficiency. In this study we focus with synthetic jet control, its success as an active flow control device has been extensively reported by several authors [1, 2, 3, 4]. This actuator is introduced inside the airfoil and is formed by a cavity with a diaphragm that oscillates in a determined frequency in order to produce a desired type of excitation. This excitation actuates with the flux adding or subtracting momentum on it in order to move the separation backwards to the trailing edge. Therefore, the laminar boundary take up more airfoil's domain and the aerodynamic performances are improved.

As the airfoil efficiency is improved better performance in crucial operations of take off and landing is achieved. However, the effectiveness of control in mitigating boundary separation depends on a number of parameters related both to the flow itself and the control input such as: frequency and amplitude of the excitation, the excitation shape, exit diameter and cavity shape. Since the synthetic jet system has several degrees of freedom and the flux is unpredictable, multiple simulations have to be done in order to assess thoroughly the best configuration to achieve the maximum airfoil's efficiency.

Nevertheless, each simulation takes a huge amount of time approximately a week and requires high computational power. For this reason, the simulations are sent to the school cluster and since each simulation requires a considerably amount of time the simulation domain have to be delimited. This study is focused on two types of excitation: continuous and periodic. The first one the amplitude of the excitation remains constant with time and the second one instead of continuous excitation the amplitude evolve with time in a particular frequency. The frequency used to simulate periodic excitation is the main frequency of the vortex shedding. Moreover, each excitation requires an extra input energy into the system that is characterized with the momentum coefficient. Then, the goal of this study is to assess properly this existent trade off between the improvement of aerodynamic performance and the momentum coefficient. And finally, extract deep conclusions and assess the best synthetic jet configuration where the aerodynamics performances are improved with a low momentum coefficient.

To extract suitably conclusions we pass through a thorough and intricate process. We follow an organized structure where the chapters are defined according to a dependency degree. This means, that the chapter after depends on all explained previously to it. For this reason, we opt for the following organization.

Firstly, to provide a practical extension to this study we perform the photogrammetry of an unmanned aerial vehicle, Skywalker x6. From the three-dimensional model we are able to extract the profile dimensions and finally we do a NACA approach with the pertinent dimensions that we use to perform the simulations.

Secondly, as Navier-Stokes equations do not have an analytical solution, numerical methods have to be used. For this reason, we have to simulate with a discretized surface. Moreover, as we want to implement the synthetic jet actuator we have to adapt this mesh for the synthetic jet. To adapt the mesh we have to restructure the nominal mesh and define new surfaces to have a high accuracy on the synthetic jet domain.

Thirdly, to simulate we use spectral element framework Nektar++. This software use XML format therefore, we have to make an appropriate conversion of the geometry. Then, we need a simulation setup file that specifies all the physical and numerical parameters for the simulation. Once this is done, the simulations are sent to the school cluster where some nodes are integrated to perform the simulations.

Finally, when the simulations are finished with xmgrace and paraview softwares and python scripts the results are extracted and we assess properly the improvements or drawbacks of simulations. Once the results are elaborated, properly conclusions have to be done in order to assess thoroughly the best configuration that provides good aerodynamic performance with a small momentum coefficient.

CHAPTER 1. AIRFOIL SELECTION

1.1. Reynolds number

This scientific study is limited by the Reynolds number. The Reynolds of a conventional airplane like Boeing 747 is over $2 \cdot 10^9$. As we will see in sections 2 and 3 due to restriction of the mesh, the solver, the available computational power and last but not least the complexity (turbulence models such as RANS, DES,etc.) that would suppose to simulate at the Reynolds experienced by a conventional airplane. This study is focused in a range of low Reynolds between 0 and 5500. Therefore, to perform deeper and better approximations and commit less error the simulations are based on the UAV Skywalker x6 airfoil. As the chord and the velocity is lower the Reynolds number is reduced.

- $V = 50 km/h$
- $c = 0.31 m$
- $\nu = 1.480 \cdot 10^{-5} \frac{m^2}{s}$
- Altitude=120 m
- $T_{120} = 15°\text{C}$

Keeping in mind all those parameters we obtain the following Reynolds number:

$$Re = \frac{V \cdot c}{\nu} \simeq 3 \cdot 10^5 \tag{1.1}$$

Note that the Reynolds number is reduced four degrees of magnitude. For all said above and for a practical extension at this study as we will see at the subsections of chapter 1, a three-dimensional model of Skywalker x6 airfoil is generated to perform the simulations.

1.2. Photogrammetry

First of all, to generate an accurate three-dimensional digital model the following parameters have to be determined:

- Focal length: 50 mm
- Diaphragm aperture: f/7.1
- Shutter speed: 1/100
- Sensibility (ISO): automatic

To perform a better adjustment and alignment of the photos the first three parameters are fixed and the sensibility automatic. Note that the shutter speed is too low with the aim to achieve a clear and sharp image to observe the airfoil roughness and in this way to obtain more homologous points among the images. In the other hand, due to the low shutter speed is easy to have moved images with distortions that could affect at their synchronization, for this reason we have used a tripod. What is more, we have installed three flashes to avoid shadows and therefore errors in the alignment.

To have all the image focused, the correct distance at which we take the photos have to be determined. Introducing all the parameters mentioned previously in the PhotoPills PdC calculator [5] the distance is obtained in Figure 1.1. Moreover, we asses with PhotoPills calculator the diffraction. However, with the aperture used and 24 megapixels the diffraction is not visible.

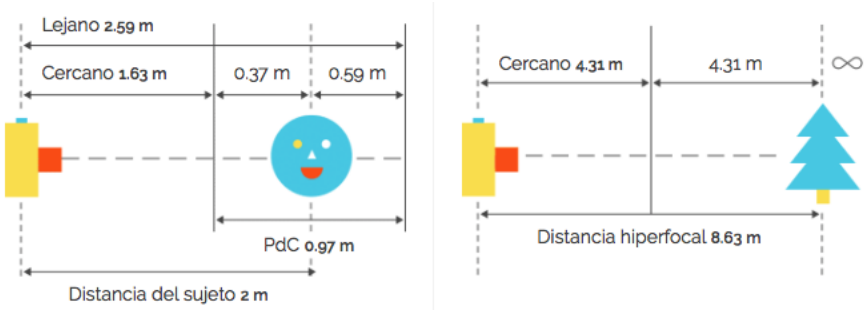

Figure 1.1: Depth of field.

Once the distance to the object is determined, the total number of photos and the different angles have to be defined. Keeping in mind that less change between photos means more homologous points found and more easily is the three-dimensional digital model generated. In this way, we take the shots in three different planes: central plane at 0°, upper and lower plane at +30°and -30° respectively. In every plane 30 photos have been taken approximately as we can observe in Figure 1.2 where in section 1.3. the connection between them and their behavior is studied.

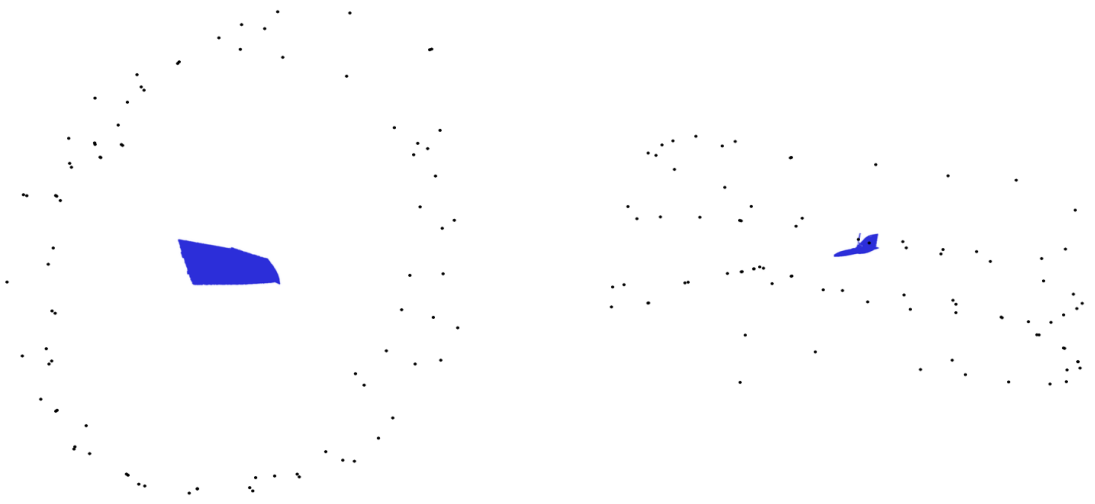

(a) Upper surface plane sight.

(b) Wing tip plane sight.

Figure 1.2: Camera location and image overlap.

1.3. Processing

The software Agisoft PhotoScan is used to process the whole set of photos. To align the photos with maximum points in common between them a scheduled process has to be followed. First of all, the interest region of the photos have to be cut. We refer to this step with doing the masks that we can observe an instance on the white line that surrounds the airfoil in Figure 1.3. Secondly, control point with the shape of bullseye or other shapes are defined. In the Figure 1.3 we can observe multiple control points.

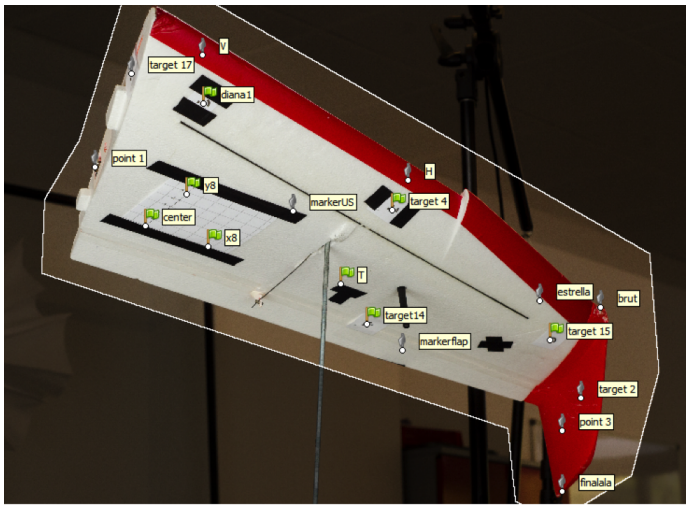

Figure 1.3: Mask and control points.

To observe more airfoil's photos we can observe them in the Appendix A.2. on Figure A.1. Following this process to each photograph, the error is reduced and the photos are aligned better having more homologous points.To scale and get the measures of the airfoil correctly a coordinates system is given. Previously, we have measured the distance between some control points and therefore introducing their coordinates to the software with an interpolate algorithm we achieve a measurable airfoil. Then, a dense cloud of points is generated, the noise is removed and we could start to mould the sketch in Figure 1.4. Moreover, in Appendix A.1. we can observe detailed information of photos alignment.

Figure 1.4: High density cloud points.

1.4. Post-processing

Once the dense cloud is generated CloudCompare is used to extract the airfoil dimensions. At Figure 1.5 we can observe the different wing sections where the chord is reduced.

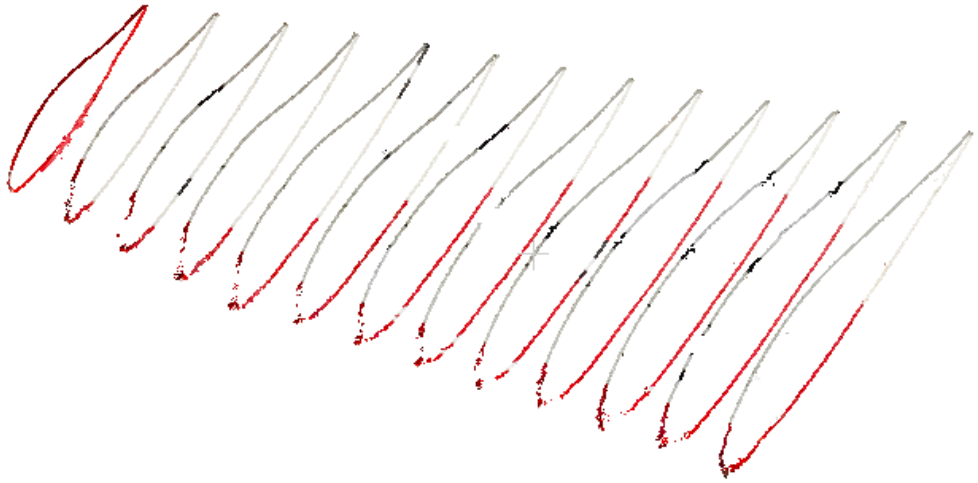

Figure 1.5: Multiple wing sections.

As we will see in section 1.5. to make a NACA airfoil approximation the following measures are needed:

- c: Chord
- P: Maximum camber
- M: Point of maximum camber
- XX: Maximum thickness

As we provide coordinates to the dense cloud we can size the airfoil and know all the measures mentioned above as we can observe in Figure 1.6:

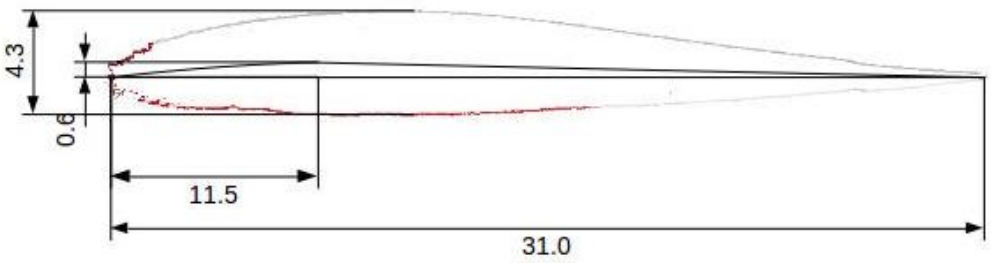

Figure 1.6: Airfoil dimensions.

1.5. NACA airfoil approximation

To build the NACA airfoil and simplify the calculations as we will see in section 3.2. we normalize the airfoil to achieve an unitary chord dimension (Figure 1.7). This is obtained dividing all dimensions by the chord calculated in section 1.4.

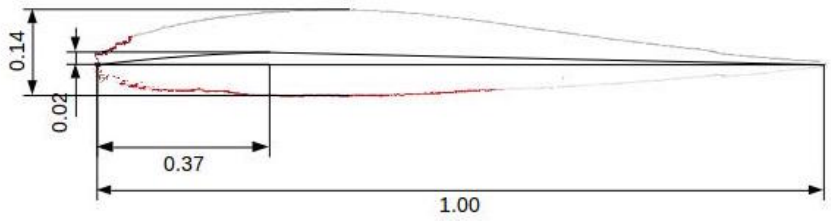

Figure 1.7: Airfoil normalized dimensions.

- c=1
- M=0.02
- P=0.37
- XX=0.14

We use the nomenclature NACA MPXX [6], therefore we obtain the NACA23714 and with the following equations 1.2-1.11 the points that form our airfoil are obtained.

$$y_t = \frac{T}{0.2} \cdot (a_0 x^{0.5} + a_1 x + a_2 x^2 + a_3 x^3 + a_4 x^4) \tag{1.2}$$

Where, $a_0 = 0.2969$, $a_1 = -0.126$, $a_1 = -0.3516$, $a_3 = 0.2843$ and $a_4 = -0.1015$ or $a_4 = -0.1036$ for closed trailing edge.

Per $0 \leq x <$p

$$y_c = \frac{M}{p^2} \cdot (2Px - x^2) \tag{1.3}$$

$$\frac{\partial y_c}{\partial x} = \frac{2M}{p^2} \cdot (2Px - x) \tag{1.4}$$

Per $p \leq x \leq 1$

$$y_c = \frac{M}{(1-p)^2} \cdot (1 - 2P + 2Px - x^2) \tag{1.5}$$

$$\frac{\partial y_c}{\partial x} = \frac{2M}{(1-p)^2} \cdot (P - x) \tag{1.6}$$

Once the camber and gradient are calculated, the points that define the upper and lower surface and so the NACA airfoil can be calculated:

$$\theta = atan(\frac{\partial y_c}{\partial x}) \tag{1.7}$$

Upper surface:

$$x_u = x_c - y_t sin(\theta) \tag{1.8}$$

$$y_u = y_c + y_t cos(\theta) \tag{1.9}$$

Lower surface:

$$x_l = x_c + y_t sin(\theta) \tag{1.10}$$

$$y_l = y_c - y_t cos(\theta) \tag{1.11}$$

Finally, applying the equations above and joining the points obtained with two lines for the upper and lower surfaces. We have found the NACA airfoil approximation (Figure 1.8) for the UAV Skywalker x6 that we use to solve the Navier-Stokes equations and where we study the synthetic jet implementation.

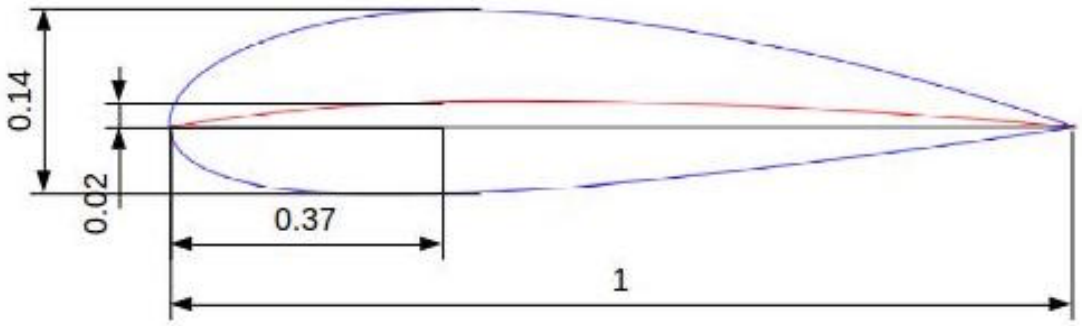

Figure 1.8: NACA airfoil approximation.

CHAPTER 2. MESH

2.1. Nominal mesh

As Navier-Stokes equations do not have an analytical solution, we have to use numerical methods to solve them. For this reason, is strongly necessary to discretize the control surface. To make it possible we use gmsh, a three-dimensional finite element mesh generator [7]. At Figure 2.1 we can analyze the discrete surface that we use to solve the Navier-Stokes equations. As we will see in section 3 this surface is split in small parts defined by the expansions.

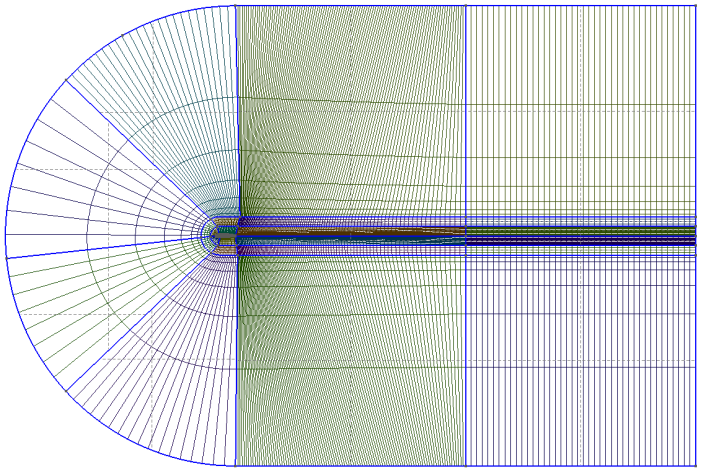

Figure 2.1: Nominal mesh.

This mesh is called c-mesh and has been tested and proven accurate to within 0.1% in producing aerodynamic forces at Re=5300 on a NACA0012 airfoil. It have to be emphasized that the mesh is completely generic, it means that if the attack angle or any parameter such as progressions, NACA parameters, line subdivisions, etc. The mesh is adjusted automatically (Figure 2.2).

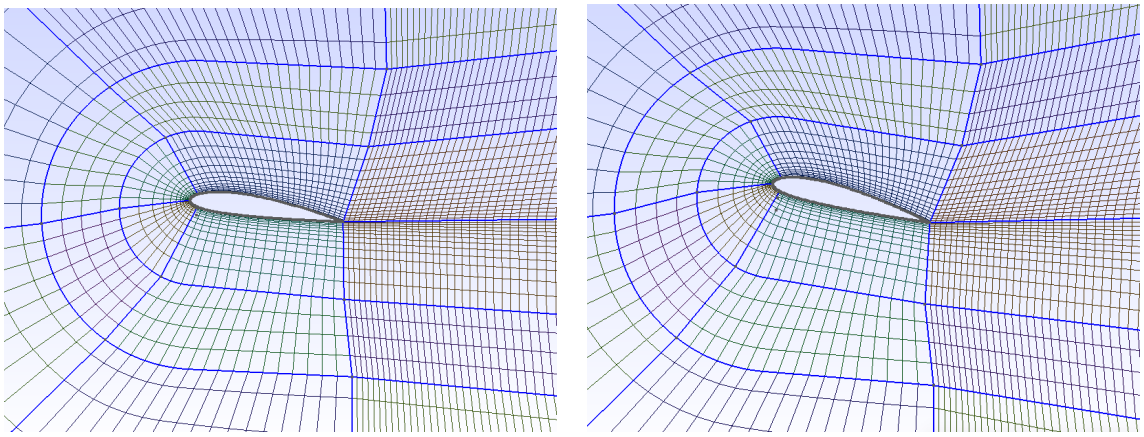

(a) Aoa = 8°

(b) Aoa = 14°

Figure 2.2: Mesh automatic adjustment when the angle of attack is changed.

First of all, the length of the first mesh element in the leading edge is defined in such a way that the length of trailing edge is four times bigger because the boundary layer is thinner at the leading edge and is increased progressively towards the trailing edge (Figure 2.3).

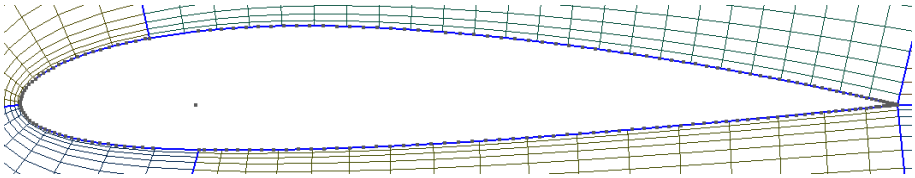

Figure 2.3: Difference between mesh element in the leading edge and the trailing edge.

Once the first elements of the mesh are established an algorithm adjust automatically the progressions, the line divisions and the shape between surfaces in a way that when the surface is changed the shape of the last mesh element is kept and is the reference for the new surface element in order to have smooth changes (Figure 2.4) and no distortions when the Navier-Stokes equations are solved.

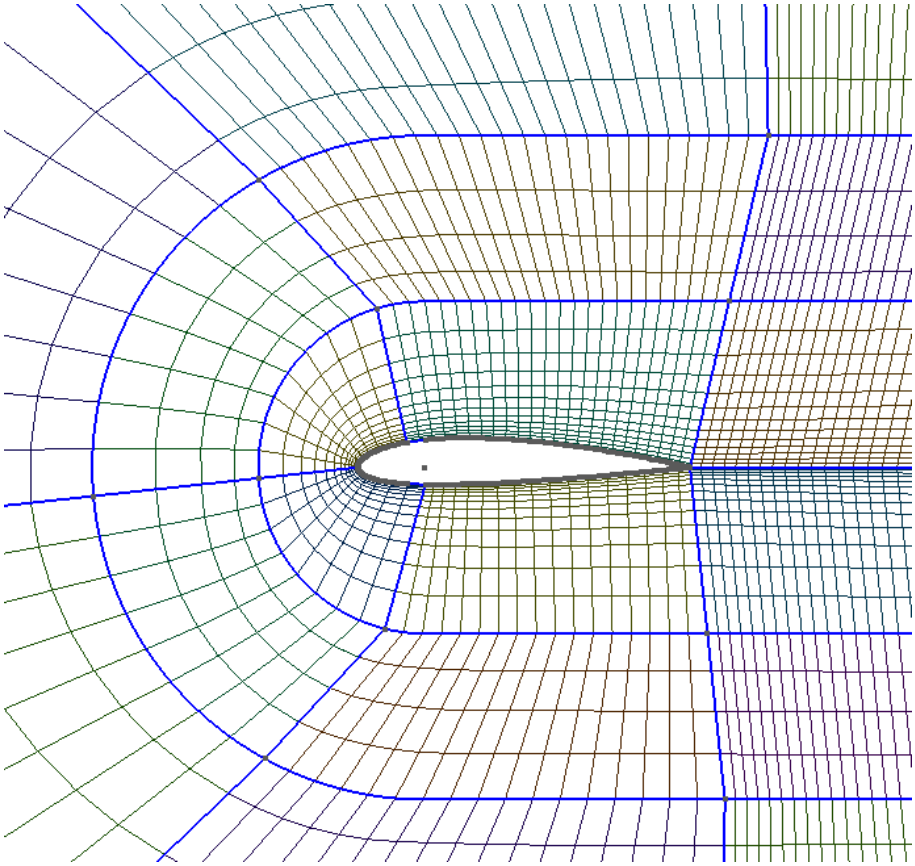

Figure 2.4: Shape conservation between surfaces.

The dimensions also have been tested, the domain extends 12, 24 and 12 chords away from the airfoil in the upstream, downstream and cross-stream directions, respectively. As we can observe at section 3.3. points closer to the mesh boundaries preserve the same values that initial conditions, therefore we can conclude that the mesh is dimensioned in an appropriate way.

This mesh is divided in the following surfaces:

- 1: Upper near field (dark blue)
- 2: Lower near field (light blue)
- 3: Wake (cyan)
- 4: Mid field except wake (green)
- 5: Upper mid field wake (yellow)
- 6: Far field (light pink)

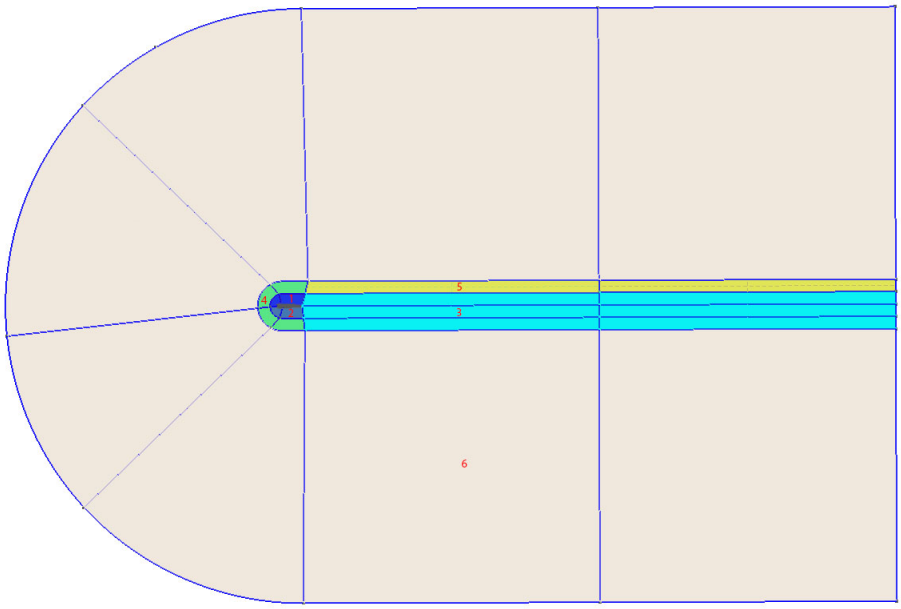

Figure 2.5: Mesh surfaces.

This division is due that in every surface different phenomena take place and each one have to be treated with different grades of accuracy. Indeed, as we comment in the beginning of this section the mesh elements that we solve are determined by the expansions that we define for each surface. We have to remark that the surface 5 is treated independently because when the attack angle is increased the wake the wake invades this region and needs to be accurately resolved.

2.2. Mesh adapted for synthetic jet implementation

As we want to study the effects of the synthetic jet we have had to modify the nominal mesh in order to mesh with more accuracy the area where the actuator is implemented. Firstly, we have had to develop an algorithm that allows to locate the synthetic jet in any place of the airfoil's upper surface and specify the jet thickness. To develop this algorithm we use gmsh [7] a three-dimensional finite element mesh generator.

The impact domain of the synthetic jet actuator is limited by a straight line where we will make special emphasis in chapter 3, while the other parts of the airfoil are joined with a curved line that goes through the points generated with the equations 1.2-1.11. We focus the implementation of the actuator only in the upper surface of the airfoil where it seems to behave better. To study the synthetic jet behavior we have generated an exclusive surface that mesh its action area. As we can observe in Figure 2.6.

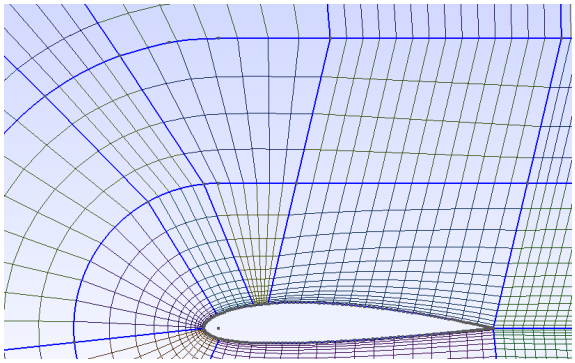

Figure 2.6: Jet synthetic mesh implementation at 20% of the chord

To preserve the continuity between mesh elements we have had to expand this surface until the mesh boundaries as we can observe in Figure 2.7.

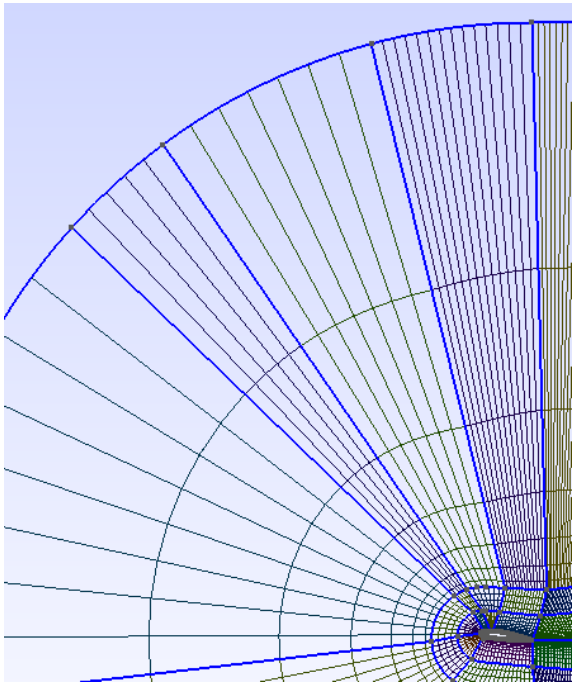

Figure 2.7: Continuity conservation between mesh elements.

Moreover, the mesh is automatically adjusted when we move the jet position over the airfoil and when the angle attack is changed as we can observe in the Figure 2.8.

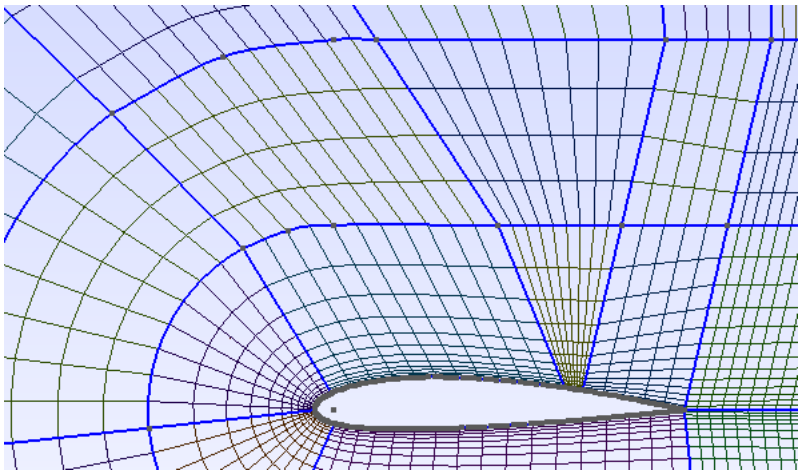

Figure 2.8: Automatic adjustment, jet location at 79% of the chord.

To perform this surfaces that extends to the boundaries we pass through several steps [7]. Firstly, we had to broke the upper surface line that joins all the points built with NACA equations in three lines. A line that goes from leading edge to jet slot, a straight line that defines the synthetic jet (Figure 2.9) and the third lines goes from the jet slot to the trailing edge. Secondly, once this partition is achieved we build two lines up until the surface boundary that are parallel to the lines that are next to each other. We repeat the second step until the boundaries. We have to take into account all the possibilities and intersections because we want to situate the synthetic jet in any location. The third step is to redefine all the line loops and name the new surfaces. The fourth step is to assign to each line the transfinite algorithm in accordance to the other surfaces to preserve the mesh element size continuity. And last but not least, we have to redefine the physic surfaces and lines. Once all the steps are followed we have almost a generic algorithm. To observe further information at the code see Appendix B.

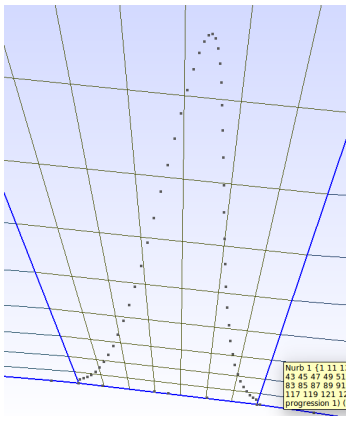

Figure 2.9: Synthetic jet excitation in the jet surface.

This mesh have some limitations that we have to take into account. We can locate the synthetic jet between 10% to 90% of the chord. Other positions can imply small distortions in the mesh. Even so, at this positions the implementation of the synthetic jet is not as important as the range available for its location. Due to this mesh we can study with high accuracy the behavior of the synthetic jet in almost all the airfoil upper surface domain.

CHAPTER 3. NAVIER-STOKES RESOLUTION

To solve the Navier-Stokes equation's we use Nektar++ spectral/hp element framework. This method divides all the elements in the mesh in nodes specified by the expansions that we specify in each mesh surface (Figure 3.1).

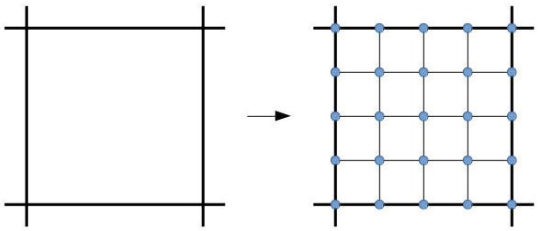

Figure 3.1: Five degree expansion.

In each node, polynomial approaches are used to solve the following equation's system:

$$\begin{cases} \frac{\partial \hat{V}}{\partial t} + \hat{V} \cdot \nabla \hat{V} = -\nabla p + v \nabla^2 \hat{V} + f \\ \nabla u = 0 \end{cases} \tag{3.1}$$

Where V is the velocity field, p is the specific pressure (including density) and v is the kinematic viscosity. This equations system is made up by Navier-Stokes and Continuity equations respectively for incompressible flux. To solve this equation system due to its complex mathematical formulation we do an easy approach, however for detailed information is better to read carefully the Nektar++ user's manual [8] where all the resolution process is explained in detail.

To solve the equation's system Nektar++ firstly uses a splitting/projection method where the velocity field and the pressure are typically decoupled. The velocity is obtained omitting the pressure. This result do not consider the continuity equation and do not conserve the mass (null divergence). Then a pressure field is computed to apply a correction to velocity that renders it solenoidal.

The Nektar++ works with file in XML format. There are three main required elements that we have to specify to the solver to perform the appropriate simulations:

- Geometry
- Expansions
- Conditions

} Conditions

To be organized we divide the input file to perform the simulation in two files. The first one we specify all the discretized surface geometry and the second one the expansions and simulation conditions are specified. Below, each file is explained in detail.

3.1. Geometry

The mesh generated with *gmsh* is converted to xml file using NekMesh. Nekmesh is a Nektar++ utility that is designed to provide a pipeline approach to mesh generation. The content of the file is structured and sorted by the following elements [8] that are ordered from low compaction to high compaction:

- Vertices: Are the whole nodes coordinates that form the mesh. In Figure 3.2 we can observe how is specified in the file.

```
1 <?xml version="1.0" encoding="utf-8" ?>
2 <NEKTAR>
3     <GEOMETRY DIM="2" SPACE="2">
4         <VERTEX>
5             <V ID="0">2.81873910e-01 9.87955574e-01 0.00000000e+00</V>
6             <V ID="1">2.77428694e-01 1.16161802e+00 0.00000000e+00</V>
7             <V ID="2">3.11133036e-01 1.16514544e+00 0.00000000e+00</V>
```

Figure 3.2: Mesh vertexs.

- Edges: Are the lines that connect every vertexes pair (Figure 3.3).

```
    <V ID="8629">2.40000000e+01 -1.22529983e+00 0.00000000e+00</V>
</VERTEX>
<EDGE>
    <E ID="0">     3  0   </E>
    <E ID="1">     2  3   </E>
    <E ID="2">     1  2   </E>
    <E ID="3">     0  1   </E>
    <E ID="4">     5  3   </E>
    <E ID="5">     4  5   </E>
```

Figure 3.3: Mesh edges.

- Elements: Are the group of edges assembled in the following geometries [8].
  - S: Segment
  - T: Triangle
  - Q: Quadrilateral
  - A: Tetrahedron
  - P: Pyramid
  - R: Prism
  - H: Hexahedron

  In our case we only have quadrilateral elements since we opt for a structured mesh (Figure 3.4).

```
        <E ID="17029"> 8629  8054   </E>
    </EDGE>
    <ELEMENT>
        <Q ID="0">    0     1     2     3 </Q>
        <Q ID="1">    4     5     6     1 </Q>
        <Q ID="2">    7     8     9     5 </Q>
        <Q ID="3">   10    11    12     8 </Q>
        <Q ID="4">   13    14    15    11 </Q>
        <Q ID="5">   16    17    18    14 </Q>
        <Q ID="6">   19    20    21    17 </Q>
```

Figure 3.4: Mesh elements.

- Composite: Is the association of elements and edges. That is because the edges define the physical lines and the elements the physical surfaces (Figure 3.5).

```
    </CURVED>
    <COMPOSITE>
        <C ID="1"> E
,14199,14281,14363,14445,14527,14609,14691,14773,14855,14937,15019,1506

        <C ID="2"> E
8424,8421,8418,8415,8412,8409,8406,8403,8400,8397,8394,8391,8388,8385,8

        <C ID="3"> E[8223,8220,8217,8214,8210] </C>
        <C ID="4"> E
1666,1668,1670,1672,1674,1676,1678,3584,3586,3588,3590,3592,3594,3596,3

        <C ID="5"> E
,12464,12461,12458,12455,12452,12449,12446,12443,12440,12437,12434,1243

        <C ID="6"> E
1349,1351,1353,1355,1357,1359,1361,1363,1365,1367,1369,1371,1373,1375,1

        <C ID="7"> E
3027,3029,3031,3033,3035,3037,3039,3041,3043,3045,3047,3049,3051,3053,3

        <C ID="8"> Q[1673-2084] </C>
        <C ID="9"> Q[4033-4344,4664-4767] </C>
        <C ID="10"> Q[3968-4032] </C>
        <C ID="11"> Q[2085-2628,4345-4460,6719-6882,7703-7866] </C>
        <C ID="12"> Q[0-1672,4461-4663,6432-6718,7416-7702] </C>
        <C ID="13"> Q[6107-6431] </C>
        <C ID="14"> Q[2629-3967,4768-6106,6883-7415,7867-8399] </C>
    </COMPOSITE>
```

Figure 3.5: Mesh composite.

- Domain: Are the physical surfaces that compose the mesh and those where the Navier-Stokes equations are solved (Figure 3.6).

```
        </COMPOSITE>
        <DOMAIN> C[8,9,10,11,12,13,14] </DOMAIN>
    </GEOMETRY>
</NEKTAR>
```

Figure 3.6: Mesh domain.

3.2. Conditions

This file contain all the simulation setup parameters. This file is divided in two main section: the expansions and the conditions [8].

3.2.1. Expansions

As we have seen in Figure 3.1, the expansions divide the mesh sub-element in nodes where the Navier-Stokes equations are solved. This section defines the polynomial expansion used on each of the defined geometric composites. Note that in Figure 3.7 the surfaces near to the airfoil have a higher degree than the far ones. Because all the important phenomena are in those regions. For this reason, they need a higher accuracy to be studied carefully and solved adequately. Nevertheless, it is important to study with close attention the trade-off between precision and time of simulation. For this reason, in section 3.3. the order of expansions is studied thoroughness.

```
<?xml version="1.0" encoding="utf-8" ?>
<NEKTAR>
    <EXPANSIONS>
        <E COMPOSITE="C[8]" NUMMODES="5" TYPE="MODIFIED" FIELDS="u,v,p" /> <!-- Upper wake -->
        <E COMPOSITE="C[9]" NUMMODES="7" TYPE="MODIFIED" FIELDS="u,v,p" /> <!-- Upper Inner Surface -->
        <E COMPOSITE="C[10]" NUMMODES="7" TYPE="MODIFIED" FIELDS="u,v,p" /> <!-- Jet -->
        <E COMPOSITE="C[11]" NUMMODES="5" TYPE="MODIFIED" FIELDS="u,v,p" /> <!-- Mid field -->
        <E COMPOSITE="C[12]" NUMMODES="5" TYPE="MODIFIED" FIELDS="u,v,p" /> <!-- Upper wake -->
        <E COMPOSITE="C[13]" NUMMODES="7" TYPE="MODIFIED" FIELDS="u,v,p" /> <!-- Lower Inner Surface -->
        <E COMPOSITE="C[14]" NUMMODES="7" TYPE="MODIFIED" FIELDS="u,v,p" /> <!-- Wake -->
    </EXPANSIONS>
```

Figure 3.7: Expansions with jet synthetic implemented.

From Figure 3.7 we can observe the composites that are specified in the domain and the interest calculation fields. As we deal with two-dimensional space we have a velocity field formed with u (axial velocity) and v (normal velocity) velocities and we also need the pressure.

3.2.2. Conditions

1. **Solver info:** The important items of solver information are the ”SOLVERTYPE”, ”EQTYPE” and ”TimeIntergationMethod” (Figure 3.8). The equation type sets the kind of equations we want to solve on the domain, in our case we deal with Navier-Stokes. The solver type sets the scheme we want to use to solve the set of equations. The time integrations method means that higher degree of the time-integration scheme, the larger the time steps can be for the same accuracy. The drawback is that the methods can become unstable and the computations diverge.

```
<CONDITIONS>
    <SOLVERINFO>
      <I PROPERTY="SOLVERTYPE"             VALUE="VelocityCorrectionScheme"/>
      <I PROPERTY="EQTYPE"                 VALUE="UnsteadyNavierStokes"    />
      <I PROPERTY="Projection"             VALUE="Continuous"              />
      <I PROPERTY="EvolutionOperator"      VALUE="Nonlinear"               />
      <I PROPERTY="TimeIntegrationMethod"  VALUE="IMEXOrder2"              />
      <I PROPERTY="Driver"                 VALUE="Standard"                />
  </SOLVERINFO>
```

Figure 3.8: Solver information.

2. **Parameters:** A lower time step means more precision but more time of simulation. To get the solution converged we need approximately 100 unit of time where one unit of time is equal to $1\ \frac{L}{U} = dt^{-1}$. Where L is the chord and U the upstream velocity.

   Then, if dt=$2 \cdot 10^{-4}$ we need 5000 time step to advance a full time unit. Therefore to have a converged simulation we need a total step number of 500000. If the synthetic jet is not implemented the time step is increased and therefore the number steps decrease as more accuracy is needed to asses properly the airfoil's domain. The IO CheckSteps is to make back-up of the simulation and IO InfoSteps is the frequency of the step information displayed.

   As we discuss in section 1.1., the Reynolds is fixed to 2500. And due to the chord is unitary and also the upstream velocity the kinematic viscosity is the inverse of Reynolds. The last four parameters are related with jet boundary conditions that are explained in boundary conditions.

```
<PARAMETERS>
  <P> TimeStep      = 0.0002   </P>
  <P> NumSteps      = 250000     </P>
  <P> IO_CheckSteps = 10000     </P>
  <P> IO_InfoSteps  = 10        </P>
  <P> Re            = 2500       </P>
  <P> Kinvis        = 1./Re     </P>
  <P> Amp           = 0.05     </P>
  <P> center        = -0.809028      </P>
  <P> var           = 0.008     </P>
  <P> theta         = 0.00596364      </P>

</PARAMETERS>
```

Figure 3.9: Simulation parameters with synthetic jet implemented.

3. **Boundaries:** We assign an ID to each boundaries that set our composites physical lines (Figure 3.10).

```
<BOUNDARYREGIONS>
  <B ID="0"> C[2] </B> <!-- Upper Surface-->
  <B ID="1"> C[3] </B> <!-- Jet-->
  <B ID="2"> C[5] </B> <!-- Lower Surface-->
  <B ID="3"> C[6,7] </B> <!-- Symmetry -->
  <B ID="4"> C[4] </B> <!-- Inlet    -->
  <B ID="5"> C[1] </B> <!-- Outlet   -->
</BOUNDARYREGIONS>
```

Figure 3.10: Boundaries with synthetic jet implemented.

4. **Variables** We assign an ID to the interested variables. In our case, u (axial velocity), v (normal velocity) and p (pressure) (Figure 3.11).

```
<VARIABLES>
  <V ID="0"> u </V>
  <V ID="1"> v </V>
  <V ID="2"> p </V>
</VARIABLES>
```

Figure 3.11: Variables.

5. **Boundary conditions**: First of all, it is important to specify what are D and N. D means Dirichlet and is a type of boundary condition where the values of the solution of Navier-Sotkes are specified in the domain limits. N is Neumann boundary condition and instead of specify the solution value, the normal derivative value is specified along the domain limits.

   In Figure 3.12 the variables values are set for all the boundaries. Region 0 and 2 are equivalent to upper and lower surfaces of the airfoil and due to the non-slip condition the values of the velocity are 0. Region 1 is equivalent to the jet surface and follows a gaussian distribution. This gaussian distribution and all the parameters associated are studied carefully in section 4.

   Region 3 make reference to the upper and lower boundary lines where the velocity is equal to the free stream velocity and is considered as far away from the domain that the normal velocity is also zero. Finally, the region 4 and 5 are the input and output boundaries respectively. As we can observe, the outlet change the Neumann and Drichlet conditions from the input where the velocity field do not have to change their value across the near domain and the pressure is set to 0 because the Navier-Stokes only depend on the pressure through its gradient.

```
<BOUNDARYCONDITIONS>
  <REGION REF="0">
    <D VAR="u" VALUE="0" />
    <D VAR="v" VALUE="0" />
    <N VAR="p" USERDEFINEDTYPE="H" VALUE="0"/>
  </REGION>
  <REGION REF="1"> <!--Jet conditions-->
    <D VAR="u" VALUE="(Amp*exp(-((x-center)^2)/(2*(var^2))))*cos(theta)" />
    <D VAR="v" VALUE="(Amp*exp(-((x-center)^2)/(2*(var^2))))*sin(theta)" />
    <N VAR="p" USERDEFINEDTYPE="H" VALUE="0"/>
  </REGION>
  <REGION REF="2">
    <D VAR="u" VALUE="0" />
    <D VAR="v" VALUE="0" />
    <N VAR="p" USERDEFINEDTYPE="H" VALUE="0"/>
  </REGION>
  <REGION REF="3">
    <D VAR="u" VALUE="1" />
    <D VAR="v" VALUE="0" />
    <N VAR="p" USERDEFINEDTYPE="H" VALUE="0"/>
  </REGION>
  <REGION REF="4">
    <D VAR="u" VALUE="1" />
    <D VAR="v" VALUE="0" />
    <N VAR="p" USERDEFINEDTYPE="H" VALUE="0" />
  </REGION>
  <REGION REF="5">
    <N VAR="u" VALUE="0" />
    <N VAR="v" VALUE="0" />
    <D VAR="p" VALUE="0" />
  </REGION>
</BOUNDARYCONDITIONS>
```

Figure 3.12: Boundary conditions.

6. **Filters**: Filters are tools that enable to extract interest data of the simulation. We principally use two types of filter, history points and forces. The first one is to extract the value of variables every time step in any place inside the domain. The second one is to extract the forces (lift and drag) acting on the surfaces. Therefore, we can analyze the behavior of each simulation and how develops during the time. Moreover, with the last filter mentioned we study the potential benefits of synthetic jet implementation.

3.3. Convergence analysis

Before simulate it is necessary to study carefully the degree of accuracy that we need. As we have said there is an important trade-off between time and precision. For this reason, we have performed different simulations with different expansion orders and time steps to assess properly the order of expansions and the time step. In this way we achieve a better efficiency reducing the time and preserving almost the same degree of accuracy.

To assess the convergence analysis we have to take a simulation like a ideal case as we can see in the Table 3.1. Then, as we can also observe from the Table 3.1 we perform other simulations named cases lowering gradually the expansions and increasing the time step. In this way, the simulations are less accurate but more quick.

	Surfaces expansions							Time Step	Total Time
	US[1]	LS[1]	Wake[1]	Jet[1]	Mid[1]	Mid Wake	Far[1]		
Reference	7	7	7	7	5	5	5	0.0002	3d 5h 45’
Case 1	5	5	5	5	5	5	5	0.0002	2d 11h 23’
Case 2	5	5	5	5	5	5	5	0.0004	1d 5h 50’
Case 3	5	5	5	5	5	5	5	0.0006	19h 28’
Case 4	5	5	5	5	3	3	3	0.0006	14h 2’
Case 5	5	5	5	5	3	3	3	0.001	6h 56’
Case 6	3	3	3	3	3	3	3	0.001	5h 20’

Table 3.1: This table shows the expansions and the time step of each case and the simulation total time.

As we supposed, when the expansions are lowered and the time step increased the total time decrease. Note, that as the time step increase and since the unit time is the inverse of time step the time step to advance a full unit of time decrease. Therefore, as the unit time decrease the total step number to have a converged simulation decrease. Due to this fact, from Table 3.1 we can observe a considerable decreasing of total time when the expansions are lowered and the time step is increased.

It is important to study the committed error in each case. As we have said we study how the aerodynamic forces differs from the reference case. For this reason, we assess both lift and drag coefficients in order the error committed between simulations.

	C_L	C_D	ε_aL	ε_aD	ε_rL [%]	ε_rD [%]
Reference	0.43215	0.12994	0	0	0	0
Case 1	0.43142	0.12983	$7,3 \cdot 10^{-4}$	$1.1 \cdot 10^{-4}$	0.169	0.085
Case 2	0.43113	0.12981	$1.02 \cdot 10^{-3}$	$1.3 \cdot 10^{-4}$	0.236	0.100
Case 3	0.43108	0.12979	$1.07 \cdot 10^{-3}$	$1.5 \cdot 10^{-4}$	0.248	0.115
Case 4	0.43035	0.12984	$1.8 \cdot 10^{-3}$	$1.0 \cdot 10^{-4}$	0.416	0.077
Case 5	0.43153	0.12987	$6.2 \cdot 10^{-4}$	$7.0 \cdot 10^{-5}$	0.143	0.054
Case 6	0.42822	0.12934	$3.93 \cdot 10^{-3}$	$6.0 \cdot 10^{-4}$	0.909	0.461

Table 3.2: Lift and drag coefficients values for each case and the error committed.

[1]The abbreviations US, LS, Jet, Mid, Far means Upper Surface, Lower Surface, Jet Surface, Mid Field and Far Field respectively.

Where, ε_a and ε_r are defined as:

$$\varepsilon_a = X_{reference} - X_{cases} \tag{3.2}$$

$$\varepsilon_r = \frac{\varepsilon_a}{X_{reference}} \cdot 100 \tag{3.3}$$

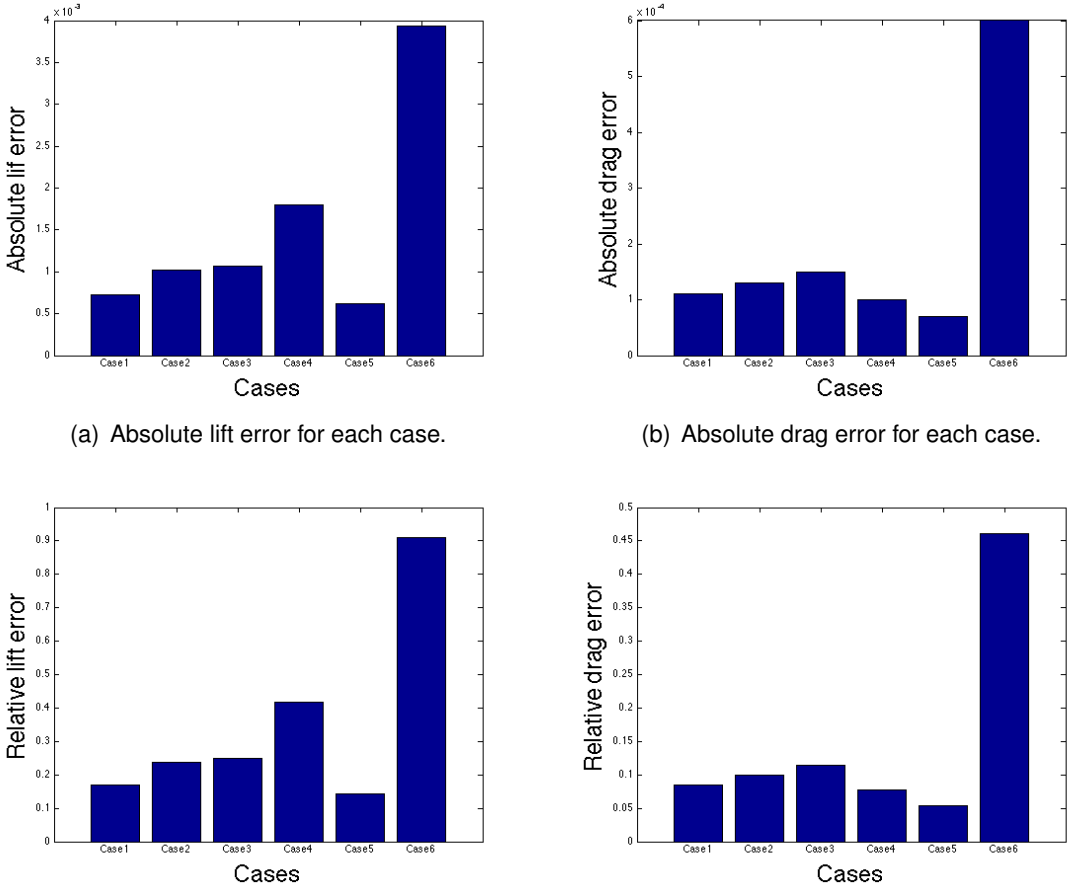

(a) Absolute lift error for each case.

(b) Absolute drag error for each case.

(c) Relative lift error for each case.

(d) Relative drag error for each case.

Figure 3.13: Errors continuous distribution.

As we can observe from Figure 3.13 the error clearly increase for case 6. The other simulations have a similar behavior and small errors except the lift in case 4 that is above the other cases. Note that the best configuration is case 5 that combines five and three degree expansions, it have small errors and small computational time.

Moreover, we want to make sure that the mesh is dimensioned in an appropriate way. Observe Appendix C.1. Figures C.1(a) and C.1(b).

CHAPTER 4. RESULTS AND DISCUSSION

The synthetic jet actuator as an active flow control depends on several parameters and therefore we have some degrees of freedom into the equations that we have to fix. First of all, we fix the excitation shape, we use a gaussian distribution because it represents adequately the synthetic jet behavior.

$$f(x \mid \mu\, \sigma^2) = A \cdot e^{-\frac{(x-\mu)^2}{2\sigma^2}} \tag{4.1}$$

Where:

- A is the gaussian amplitude
- μ is the mean or expectation of the distribution
- σ^2 is the variance

This versatile gaussian distributions allows us to change its shape easily. From this expression we will change the amplitude (A) and the jet location (μ). Secondly, the jet slot width is fixed to 0.05L where L is the chord. Once these parameters are defined we have to assess what type of boundary conditions. To perform the simulations we use two types of boundary conditions: continuous and oscillatory. We divide each boundary condition in two excitations as we can observe on the diagram below. Strictly, the jet is called to be a synthetic jet only if it is oscillatory and the net mass flux is zero over a full period. However, we call synthetic jet to the actuator that can perform other types of excitations.

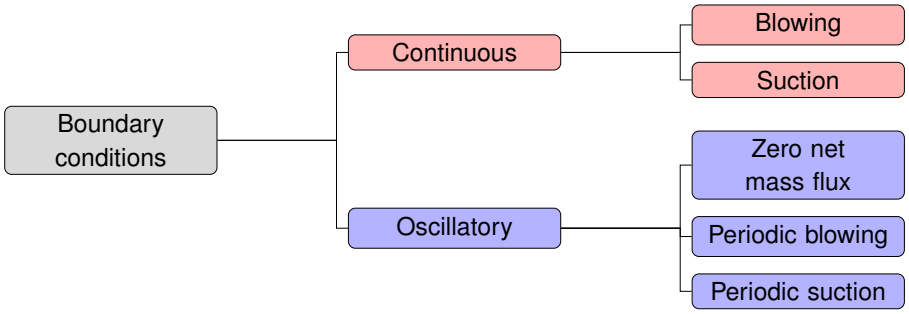

As we will see in section 4.4. we could not apply the oscillatory boundary condition at the synthetic jet.

Previously to run simulation with this types of boundary condition we perform a simulation without the inference of the jet synthetic actuator in order to know where the boundary layer separation occurs. The separation is at 0.35L form the leading edge. Therefore, we start the simulations with the jet location at 0.2L. Once the jet synthetic position is known, from section 2.2. we introduce the desired jet location and the script returns automatically the gaussian's distribution mean (μ). Moreover, the script returns the synthetic jet slope to establish the velocity field (u,v).

A decisive factor in order to choose the best boundary condition is the momentum coefficient (C_μ). The momentum coefficient is a way to quantize the extra energy that the system does in order to make the synthetic jet work. Each type of excitation requires more or less

energy, therefore the momentum coefficient is a way to assess if the excitation is expensive in terms of energy. Moreover, as it is a non dimensional coefficient the results can be compared from other type of experiments. From several articles [9, 10, 2, 4] we observe that the momentum coefficient is defined as:

$$C_\mu = \frac{\overline{I_j}}{\frac{1}{2}\rho_o {U_o}^2 c} \tag{4.2}$$

Where:

$$\overline{I_j} = \frac{1}{\tau}\rho_j b \cdot \int_0^\tau u_j^2(t)dt \tag{4.3}$$

Where:

- τ is the period of the diaphragm
- ρ_j is the synthetic jet fluid's density
- b is the synthetic jet width
- $\frac{1}{\tau}\int_0^\tau u_j^2(t)dt$ is phase averaged velocity

We need to calculate the phase averaged velocity:

$$u_j(x,t) = A(t) \cdot e^{-\frac{(x-\mu)^2}{2\sigma^2}} \tag{4.4}$$

$$b \cdot u_j^2(t) = \int_{\mu-\frac{b}{2}}^{\mu+\frac{b}{2}} A^2(t) \cdot e^{-\frac{(x-\mu)^2}{\sigma^2}} dx \tag{4.5}$$

Making the following variable change:

$$\xi = \frac{x-\mu}{\sigma} \tag{4.6}$$

$$d\xi = \frac{dx}{\sigma} \rightarrow dx = \sigma d\xi \tag{4.7}$$

As the gaussian distribution is symmetric and with the variable change we obtain:

$$b \cdot u_j^2(t) = 2 \cdot \sigma \cdot A^2(t) \cdot \int_0^{\frac{b}{2\sigma}} e^{-\xi^2} d\xi \tag{4.8}$$

The equation 4.8 is very similar to the error function 4.9:

$$erf(x) = \frac{2}{\sqrt{\pi}} \int_0^x e^{-t^2} dt \tag{4.9}$$

Therefore:

$$b \cdot u_j^2(t) = 2 \cdot \sigma \cdot A(t)^2 \cdot \int_0^{\frac{b}{2\sigma}} e^{-\xi^2} d\xi = \sqrt{\pi} \cdot \sigma \cdot A^2(t) \cdot erf(\frac{b}{2\sigma}) \tag{4.10}$$

Once the velocity is calculated on the gaussian distribution we can obtain the momentum coefficient:

$$C_\mu = \frac{\frac{1}{\tau}\rho_j \cdot \int_0^\tau \sqrt{\pi}\cdot\sigma\cdot A^2(t)\cdot erf(\frac{b}{2\sigma})dt}{\frac{1}{2}\rho_o {U_o}^2 c} \tag{4.11}$$

As the ρ_j and ρo are the same:

$$C_\mu = \frac{2\sqrt{\pi}\cdot\sigma\cdot erf(\frac{b}{2\sigma})\cdot\int_0^\tau A^2(t)dt}{\tau {U_o}^2 c} \tag{4.12}$$

Finally, we can approximate a momentum coefficient for each boundary condition. If it is continuous, the amplitude do not have temporal dependency and therefore:

$$C_\mu = \frac{2\sqrt{\pi}\cdot\sigma\cdot A^2\cdot erf(\frac{b}{2\sigma})}{{U_o}^2 c} \tag{4.13}$$

If the boundary condition is oscillatory then we can not omit the amplitude. We have to study how the amplitude evolve with time and resolve the integral with the amplitude time dependency as equation 4.12.

On the continuous boundary condition we apply a permanent excitation that do not vary with time. The amplitude of the excitation is not temporal dependent and remains constant in the whole simulation. We divide in two types of excitation the continuous boundary condition that are: blowing and suction. Both excitations keep a variance of 0.008 and a Reynolds number of 2500 as we mentioned on section 1.1.. In Figure 4.1 we can observe both types of excitation as well as the simulation amplitudes that we perform for each excitation.

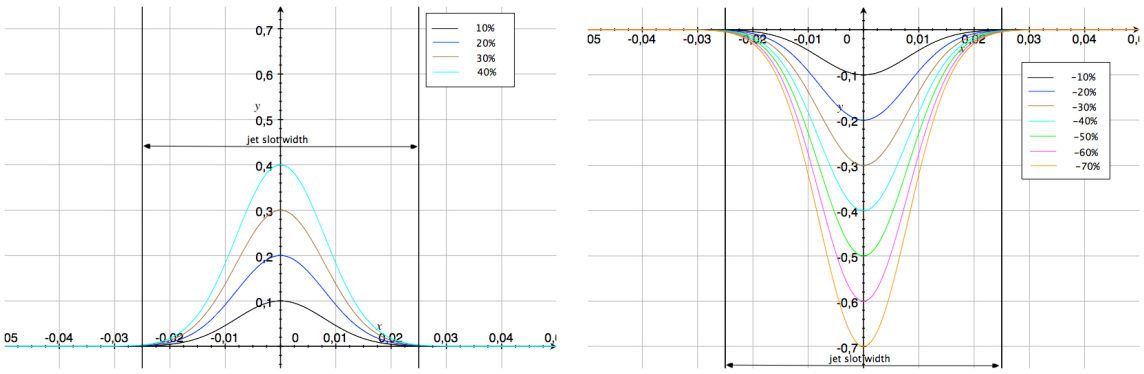

(a) Blowing excitation.

(b) Suction excitation.

Figure 4.1: Continuous excitations.

4.1. Suction

Several simulations are performed increasing the suction amplitude to observe how the flux evolve at. Once all the simulations are performed we are available to extract detailed results. First of all, we assess properly the aerodynamic forces. Secondly, the wall shear stress that actuate in the upper surface. Thirdly, the pressure distribution around the airfoil. Then the viscous and pressure drag and finally, the frequencies spectrum.

4.1.1. C_L vs C_D

As we explained in section 3.2.2. due to the filters we are able to extract the aerodynamic forces from the desired surfaces. From the filter we obtain the lift and drag forces, nevertheless, we want to work with dimensionless lift and drag coefficient. To represent both coefficient a previous step has to be done:

$$C_L = \frac{2L}{\rho_o U_0^2 c} \tag{4.14}$$

$$C_D = \frac{2D}{\rho_o U_0^2 c} \tag{4.15}$$

As all denominator factors are unitary we obtain:

$$C_L = 2L \tag{4.16}$$

$$C_D = 2D \tag{4.17}$$

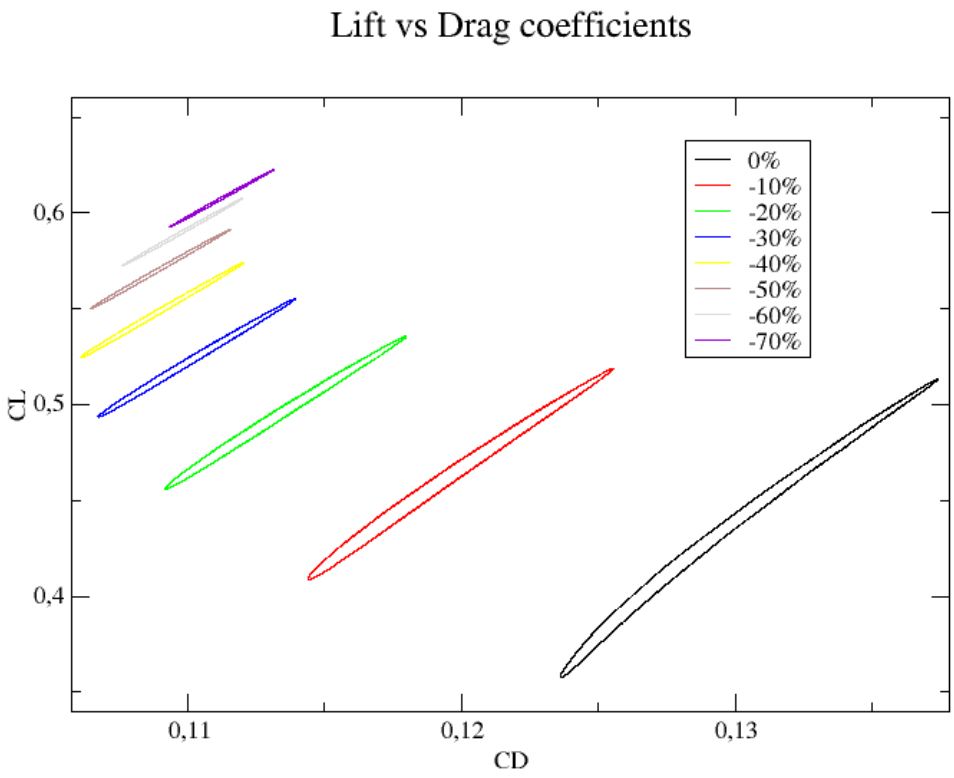

Figure 4.2: Lift vs drag coefficients for different suction amplitudes.

	C_L	C_D	σ_L	σ_D	e[2]
0%	0.4311	0.1297	0.0552	0.0049	3.3233
-10%	0.4618	0.1196	0.0384	0.0039	3.8612
-20%	0.4947	0.1134	0.0282	0.0031	4.3624
-30%	0.5237	0.1102	0.02180	0.0025	4.7522
-40%	0.5489	0.1090	0.0176	0.0021	5.0357
-50%	0.5704	0.1089	0.0146	0.0018	5.2378
-60%	0.5898	0.1097	0.0124	0.0015	5.3765
-70%	0.6074	0.1112	0.0106	0.0013	5.4622

Table 4.1: Detailed results for each suction amplitude. The ”e” superindex is misleading it refers to the footnote at the bottom of the page.

As we can observe from Figure 4.2 and Table 4.1 as we increase the suction amplitude the lift coefficient is increased and the drag coefficient is reduced except for suction of -70% where the drag coefficient is increased. This anomaly is observed below when we assess the drag in detail. Moreover, we can observe that lift and drag standard deviation are reduced when the suction amplitude is increased. This suppose less oscillation since the vortex shedding amplitude is reduced. This reduction have a direct relation with the separation point that is studied with the wall shear stress.

Besides, from Table 4.1 we observe that the efficiency (e) calculated as lift and drag coefficients ratio increase with suction amplitude. We get that the suction of -70% of the initial velocity is the best configuration in terms of efficiency.

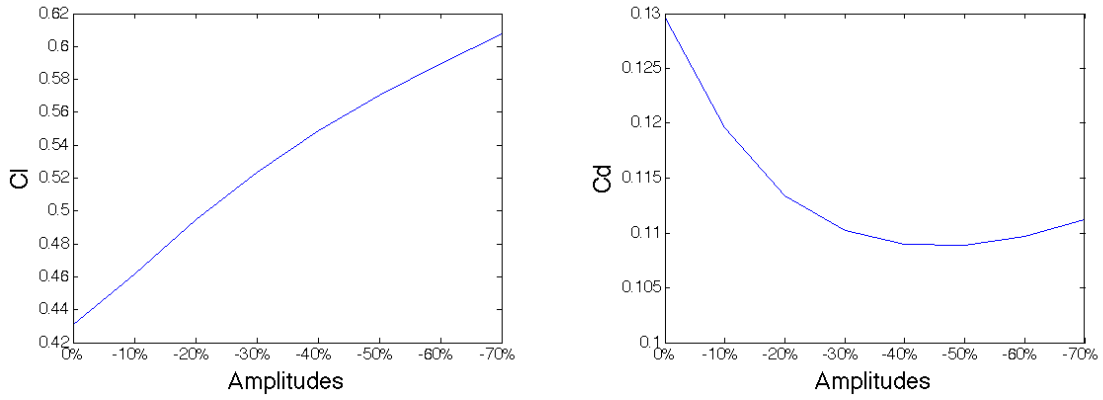

(a) Lift coefficient for different amplitudes evolution.

(b) Drag coefficient for different amplitudes evolution.

Figure 4.3: Lift and drag coefficients trend for different suction amplitudes evolution.

[2]e is the efficiency calculated as the ratio between lift and drag coefficients

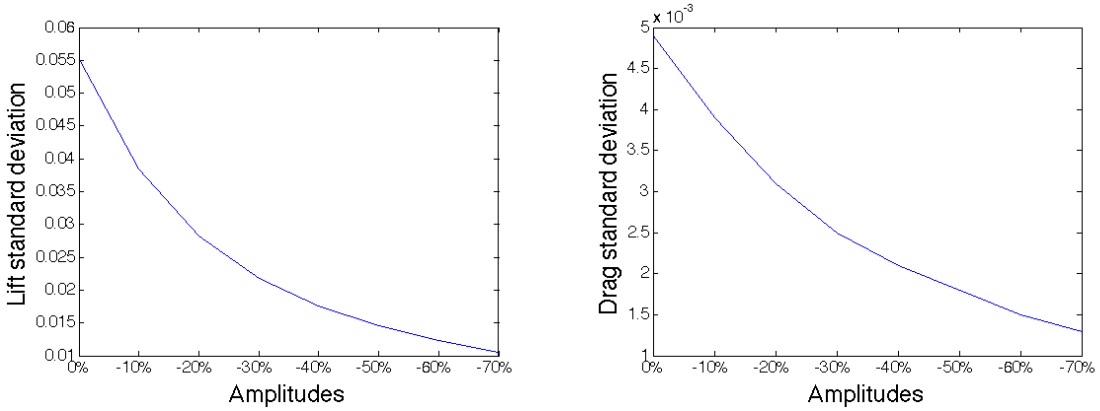

(a) Lift standard deviation for different amplitudes. (b) Drag standard deviation for different amplitudes.

Figure 4.4: Lift and drag coefficients standard deviations trend for different suction amplitudes.

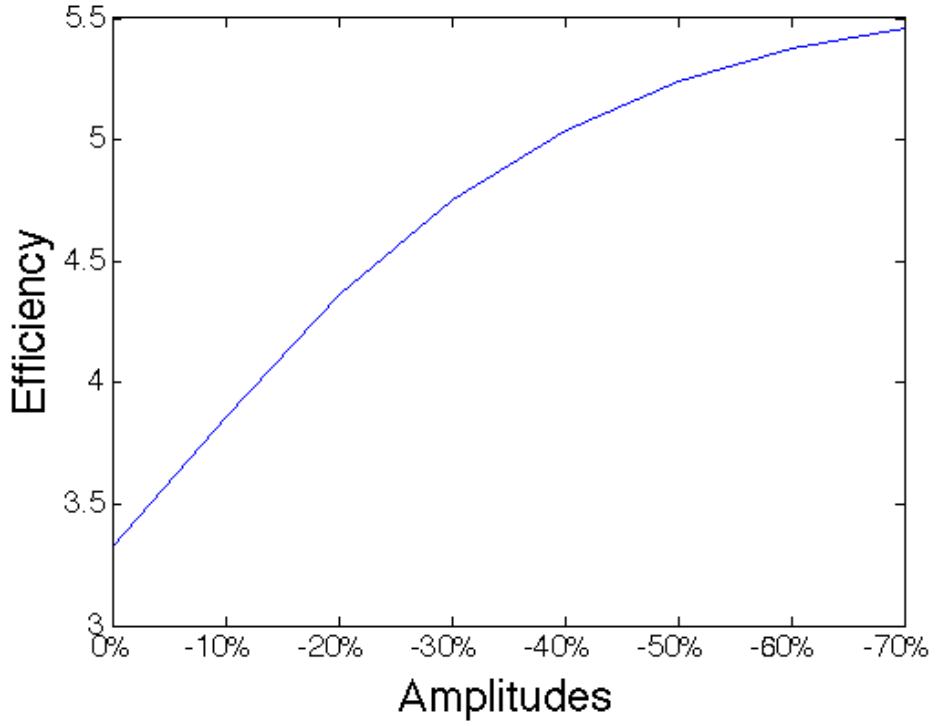

Figure 4.5: Efficiency trend for different suction amplitudes.

4.1.2. Wall shear stress

All this improvements are due to the boundary layer behavior and the pressure distribution. As we increase the suction amplitude the separation point tends to move backwards to the trailing edge as we can observe from Figure 4.6.

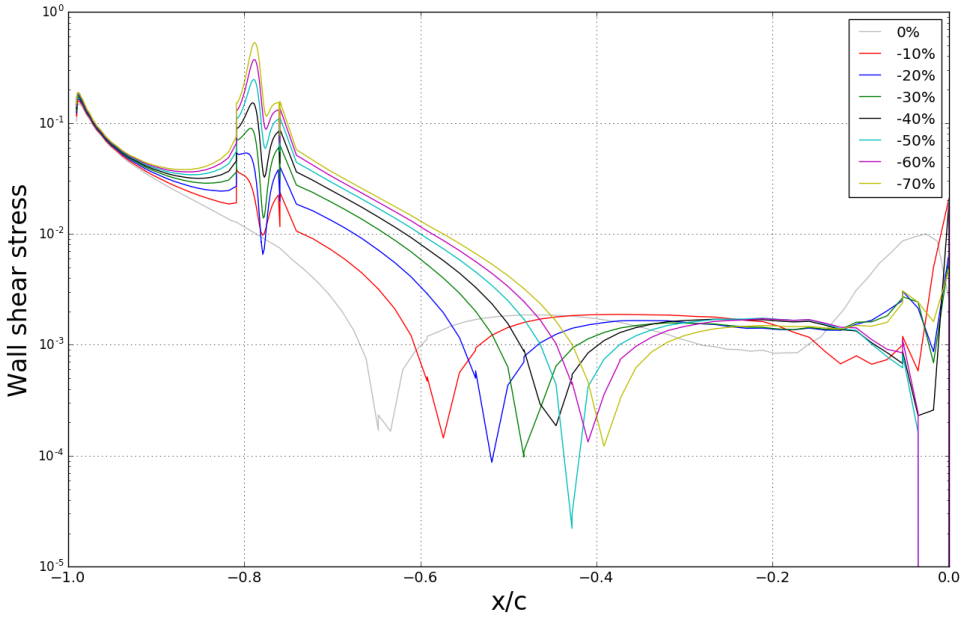

Figure 4.6: Wall shear stress across the upper surface for each simulation.

On Figure 4.6, we can observe clearly how the separation points tends to move backwards. The separation point is delayed until 0.60L that corresponds to the -70% configuration. This means more leverage of the upper surface and smaller detachment area. For this reason, lift and drag improvements are achieved. An other significant detail from Figure 4.6 is that in the position equals to -0.78 we can appreciate small fluctuations on the wall shear stress that are due to the synthetic jet. Supposedly, this is due to the fact that the gaussian distribution is not a closed curve in the jet domain. Instead, the gaussians domain is infinity, therefore, as the gaussian curve is open we have an abrupt change on the wall shear stress graph.

Besides, this separation delay also can be assessed (Figure 4.7) computing the velocity field in the paraview software and applying the streamline algorithms.

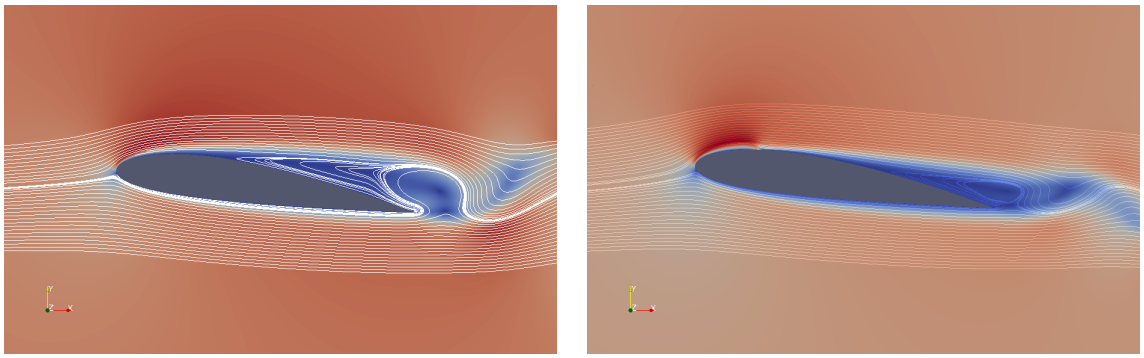

(a) Nominal case without synthetic jet implementation.

(b) Synthetic jet with a suction amplitude of 70%

Figure 4.7: Airfoil streamlines.

As we see in Figure 4.7(a) we have a huge recirculation zone that is spreaded until the separation point. However, in Figure 4.7(b) this recirculation zone has decreased and positioned backwards. For further information and more streamlines photos see Appendix C.2.1.

This wall shear stresses are from an instantaneous time. As we know due to the vortex shedding the values can vary in time. For this reason, we want to compute the average wall shear stress for each amplitude for one vortex shedding cycle to assess the variation produced by the vortex shedding.

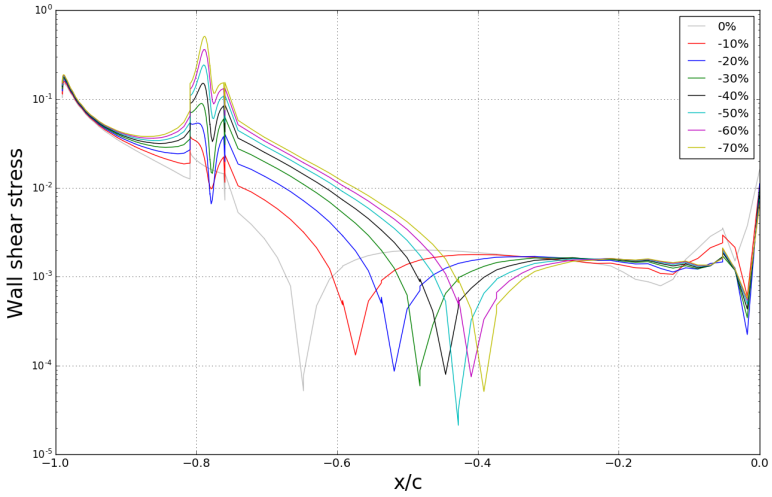

Figure 4.8: Wall shear stress average for different suction amplitudes.

From Figure 4.8 we observe that the separation occurs at the same point. To see it better we put both instantaneous and average wall shear stresses separations in terms of the chord in Table 4.2.

	$wss^3{}_{instantaneous}$	$wss^3{}_{average}$
0%	0.3517L	0.3528L
-10%	0.4260L	0.4260L
-20%	0.4813L	0.4823L
-30%	0.5174L	0.5184L
-40%	0.5545L	0.5535L
-50%	0.5726L	0.5726L
-60%	0.5917L	0.5907L
-70%	0.6098L	0.6087L

Table 4.2: Detailed results from viscous and pressure drag.

From Table 4.2 we can observe that the values do not differ to much from each other. Therefore, to avoid complications and more simulations we work with the instantaneous wall shear stress. Moreover, on Appendix C.2.3. Figure C.5 we can observe the vortex shedding evolution at one cycle.

[3] wss refers to wall shear stress

4.1.3. Pressure distribution

As we say before, the pressure distribution around the airfoil upper and lower surfaces have a significance on the improvements.

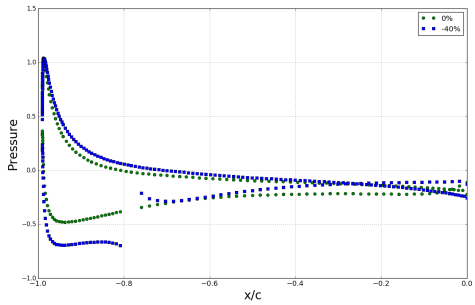

(a) Pressure distribution around upper and lower surface for suctions of 0% and -40%.

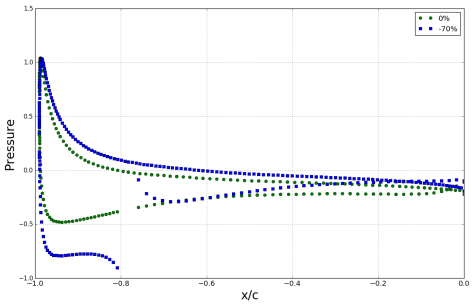

(b) Pressure distribution around upper and lower surface for suctions of 0% and -70%.

Figure 4.9: Pressure distribution.

From Figure 4.9(b) and 4.9(a) we can observe that higher pressures are achieved on the lower surface and lower pressures at the upper surface. As the difference is bigger we get a lift improvement. This improvement on lift is mainly achieved between positions 0.2L and 1L that corresponds to the jet location. After the jet slot the pressure distribution on the upper surface tends to behave worse than the nominal case. Moreover, we can observe that the difference on pressures is bigger on Figure 4.9(b) than Figure 4.9(a), therefore, a high lift is achieved with a suction amplitude of 70%. To observe the pressure distribution for the other suction amplitudes see Appendix C.2.2.

4.1.4. Viscous vs pressure drag

Drag is formed by the pressure drag or form drag and viscous drag or skin friction. Pressure drag depend on the object shape, pressure distribution and Reynolds number. The general size and shape of the body are the most important factors in form drag; bodies with a larger presented cross-section will have a higher drag than thinner bodies; sleek ("streamlined") objects have lower form drag. Viscous drag also depends on the geometry and Reynolds number and is due to the friction between the fluid and the airfoil's surface.

	D_V	D_P
0%	0.0263	0.0384
-10%	0.0272	0.0325
-20%	0.0287	0.0279
-30%	0.0306	0.0244
-40%	0.0327	0.0217
-50%	0.0350	0.0194
-60%	0.0373	0.0175
-70%	0.0398	0.0157

Table 4.3: Detailed results from viscous and pressure drag.

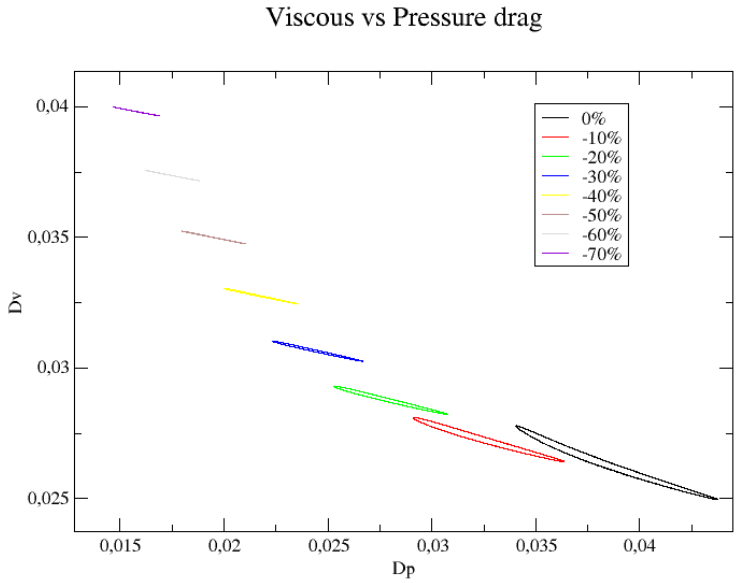

Figure 4.10: Viscous drag vs pressure drag for different suction amplitudes.

As we see from Figure 4.10 and Table 4.3 while the suction amplitude is increased the pressure drag is reduced and the viscous drag is increased. This is due to the delay of the separation point. As the separation point moves backwards the total wall shear grow and therefore, the viscous drag is increased and since the separation point occurs backwards the flow is more attached and the pressure drag decrease. Note that on Figure 4.2 and Table 4.1 the drag have a slight increase for a suction of -70% free stream velocity. To have a better understanding of how drag evolve we perform the Figure 4.11.

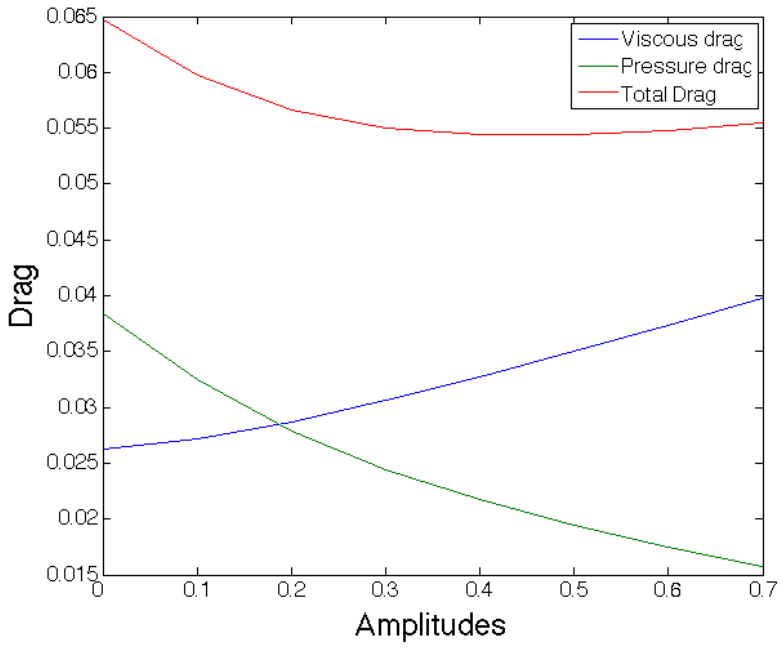

Figure 4.11: Viscous drag vs pressure drag for different suction amplitudes.

We observe that the evolution of drag is not linear and tends to be more quadratic. The minimum drag is accomplished between amplitudes of 40% and 50% then tends to increase again.

4.1.5. Vortex shedding frequency

An other interesting fact is the vortex shedding frequency reduction. Due to the Fourier transform performed with xmgrace software we can assess properly the period evolution of vortex shedding ejection.

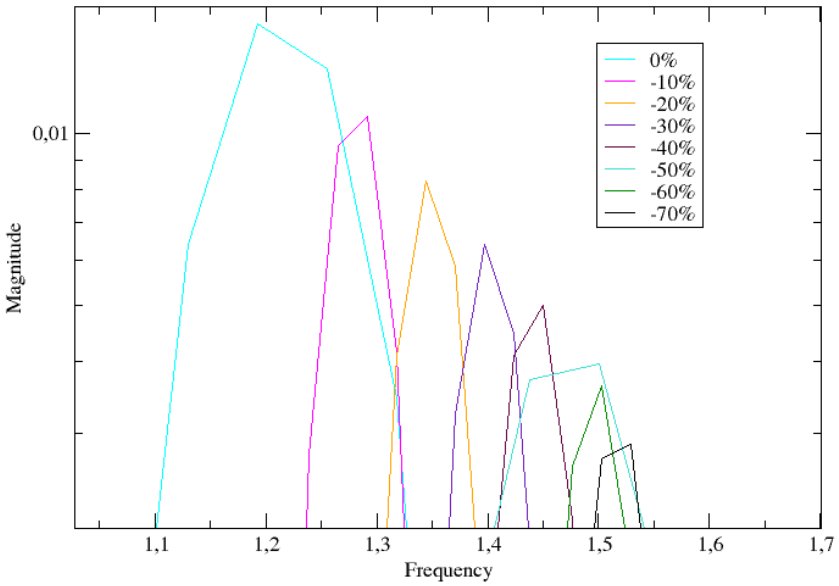

Figure 4.12: Vortex shedding first harmonic frequencies for different suction amplitudes.

	Frequency
0%	1.2120
-10%	1.2935
-20%	1.3464
-30%	1.3967
-40%	1.4503
-50%	1.4754
-60%	1.5034
-70%	1.5287

Table 4.4: Frequency values for the different suction amplitudes.

We can observe from Figure 4.12 and Table 4.4 a clear frequency reduction when the suction amplitude is increased. This means that the vortex shedding are ejected with more temporal spacing between them and therefore, the wake is less turbulent.

4.1.6. Momentum coefficient

From all seen above, we clearly observe the positive evolve when the suction amplitude is increased. However, all this improvements have an external cost to the system that we characterize with the jet momentum coefficient with equation 4.13. Substituting the parameters we obtain:

$$C_\mu = 2\sqrt{\pi}\cdot\sigma\cdot A^2\cdot erf(\frac{b}{2\sigma}) \tag{4.18}$$

$$C_\mu = 0.1772\cdot A^2 \tag{4.19}$$

Therefore, applying the equation 4.19 we obtain the following distribution:

	C_μ
0%	0
-10%	$1.8\cdot10^{-3}$
-20%	$7.1\cdot10^{-3}$
-30%	$1.6\cdot10^{-2}$
-40%	$2.84\cdot10^{-2}$
-50%	$4.43\cdot10^{-2}$
-60%	$6.38\cdot10^{-2}$
-70%	$8.68\cdot10^{-2}$

Table 4.5: Momentum coefficient for the different suction amplitudes.

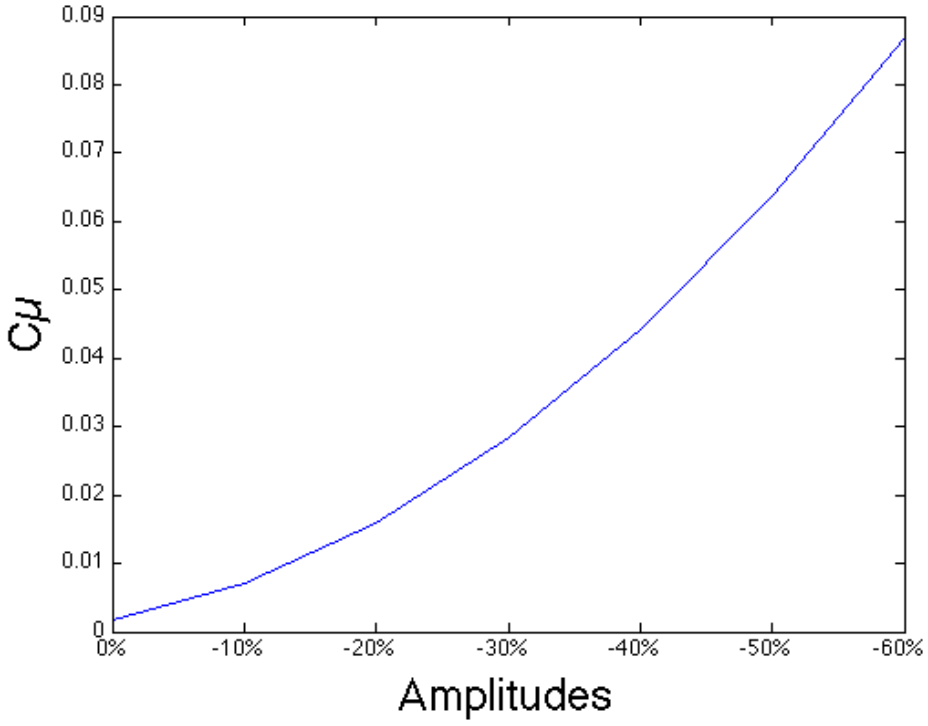

Figure 4.13: Momentum coefficient trend for different suction amplitudes.

From Figure 4.13 and Table 4.5 we observe that the momentum coefficient is increased when the suction amplitude also increase.

As we have said at the beginning of section 4 we situate the jet slot at 0.2L. As the separation occurs at 0.35L we want to study the effect of moving the jet slot at 0.3L closer to the separation point. As this study goes out our range of simulations a brief explanation of the main results is done. Only one simulation of suction amplitude 10% was performed at this location and below we compare it between the nominal case and 10% of suction amplitude at 0.2L.

4.1.7. Suction at 0.3L

Firstly, we start with the aerodynamic forces coefficients assessment.

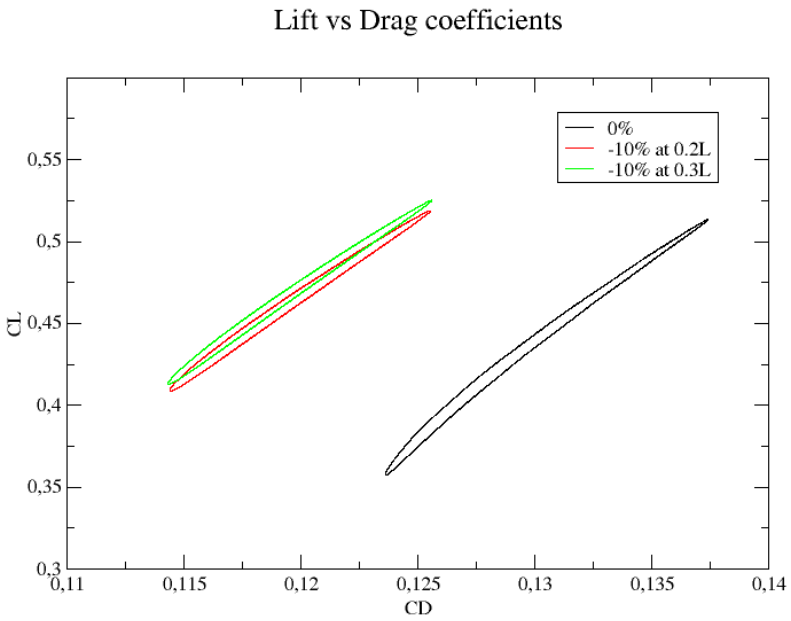

Figure 4.14: Lift vs drag coefficients for different amplitudes and locations.

	C_L	C_D	σ_L	σ_D	e
0%	0.4311	0.1297	0.0552	0.0049	3.3233
-10% at 0.2L	0.4619	0.1196	0.0389	0.0040	3.8620
-10% at 0.3L	0.4672	0.1196	0.0398	0.0040	3.9063

Table 4.6: Detailed results for each amplitude.

As we can observe from Figure 4.14 and Table 4.6 the lift increase a little bit from the suction at 0.2L, the drag is the same and the standard deviations are practically the same too. There are no big changes respect to the previous jet slot location. Nevertheless, to dissipate any doubt it would be good to study the trend when the suction amplitude at 0.3L is increased.

If we assess the wall shear stress from Figure 4.15 we observe confusing results.

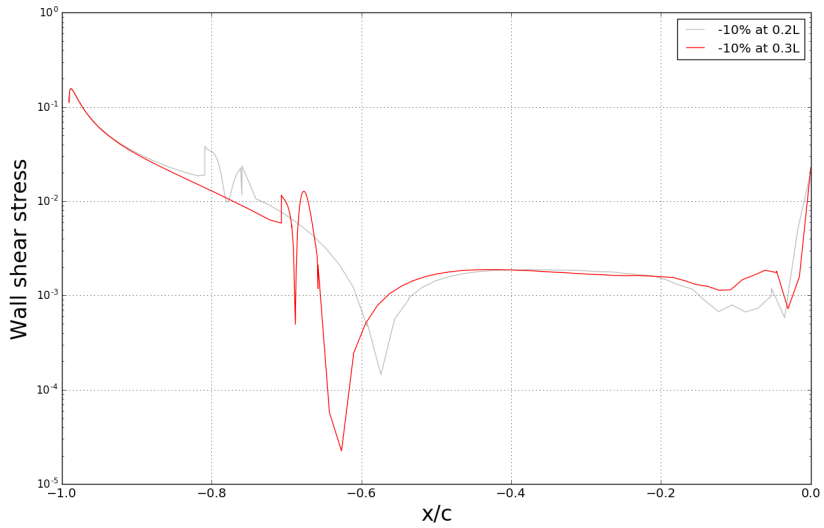

Figure 4.15: Wall shear stress across the upper surface for each simulation.

As the aerodynamic performances at 0.3L improve a little we expect that the separation move backwards. Instead, the separation occurs early to the leading edge. Because this analysis is given in an instantaneous time it do not contemplate the wall shear stress variance due to the vortex shedding oscillation. To have reliable results we should compute the average wall shear stress during one vortex shedding cycle.

From Figure 4.16 we obtain a similar pressure distribution that corroborates the small changes in the aerodynamic performance.

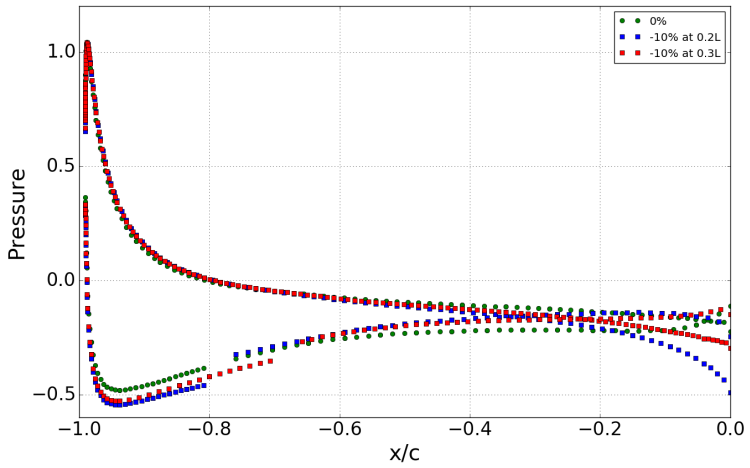

Figure 4.16: Pressure distribution for the different amplitudes

To conclude, as we do not get a significant improve on the aerodynamic forces and the momentum coefficient is the same we preserve the jet slot location at 0.2L for the further simulations.

4.2. Blowing

Instead of simulate with suction amplitudes this type of excitation is the other way around. Is based on injecting air and therefore momentum to the flux. We do the same assessment than in suction for the blowing excitation.

4.2.1. C_L vs C_D

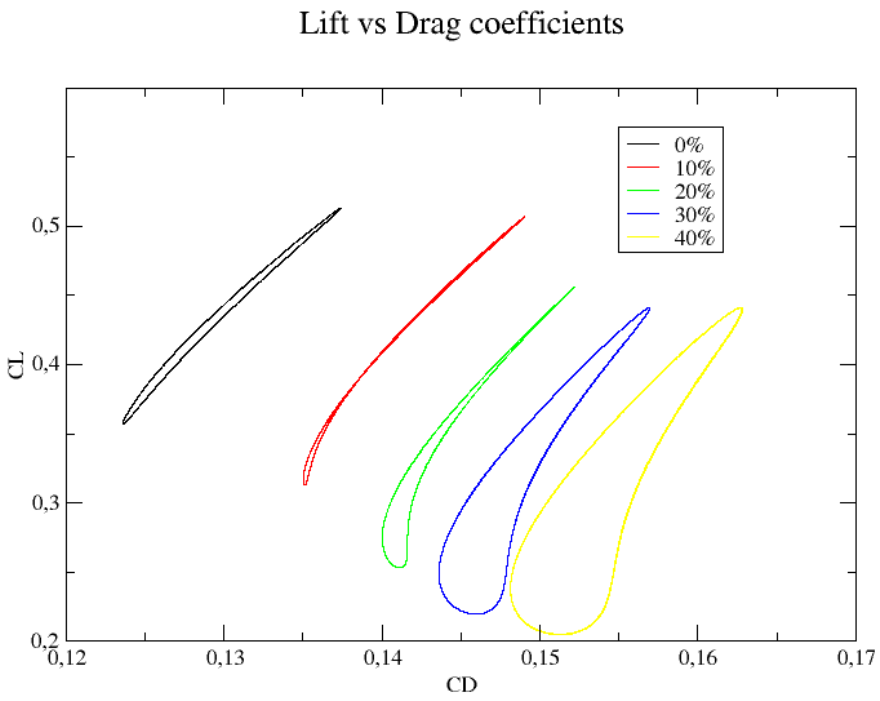

Figure 4.17: Lift vs drag coefficients for different blowing amplitudes.

	C_L	C_D	σ_L	σ_D	e^2
0%	0.4311	0.1297	0.0552	0.0049	3.3233
10%	0.4004	0.1403	0.0691	0.0051	2.8538
20%	0.3447	0.1447	0.0724	0.0042	2.3821
30%	0.3199	0.1494	0.0791	0.0043	2.1412
40%	0.3120	0.1550	0.0842	0.0047	2.0129

Table 4.7: Detailed results for each blowing amplitude.

From Figure 4.17 and Table 4.7 we observe a considerably degradation of the aerodynamic performance. When the amplitude is increased the lift coefficient decrease and the drag coefficient increase lowering the airfoil's efficiency. Moreover, the vortex shedding amplitude is increased as we can observe the lift standard deviation from Table 4.7.

4.2.2. Wall shear stress

As we know the aerodynamic performance have a direct link with the boundary layer behavior. As the conditions get worse we expect that the separation point moves forward to the leading edge.

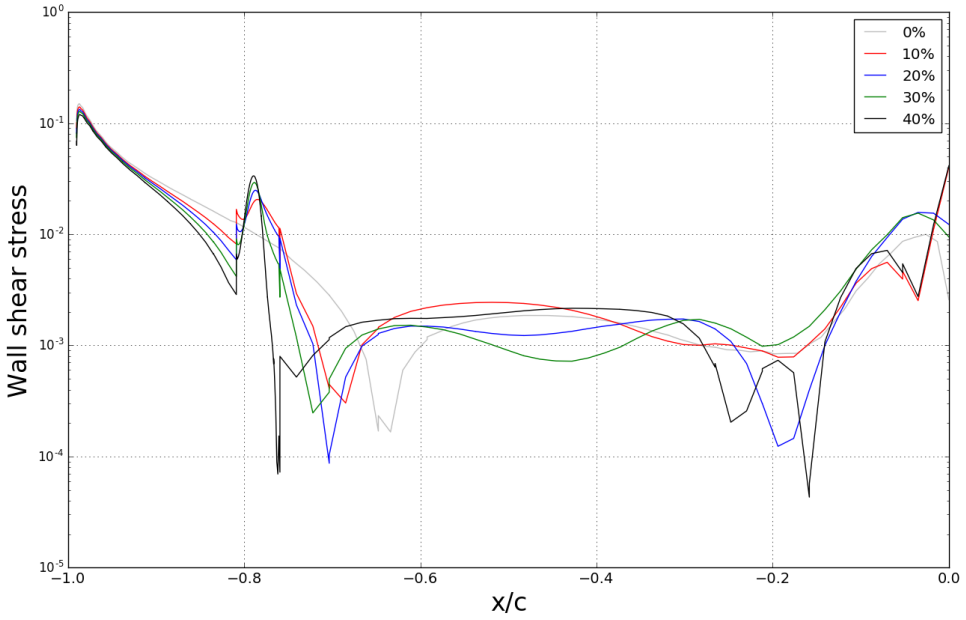

Figure 4.18: Wall shear stress across the upper surface for each simulation.

As we said above, from Figure 4.18 we can observe that the separation point clearly moves forward until the jet slot. Nevertheless, for amplitudes of 20% and 40% seems that the flux is reattached again. But, if we make a close look to the Figure 4.19(b) there is a huge recirculation zone and therefore the reattachment hypothesis is not considered. For more streamline images see Appendix C.3.1. Figure C.6.

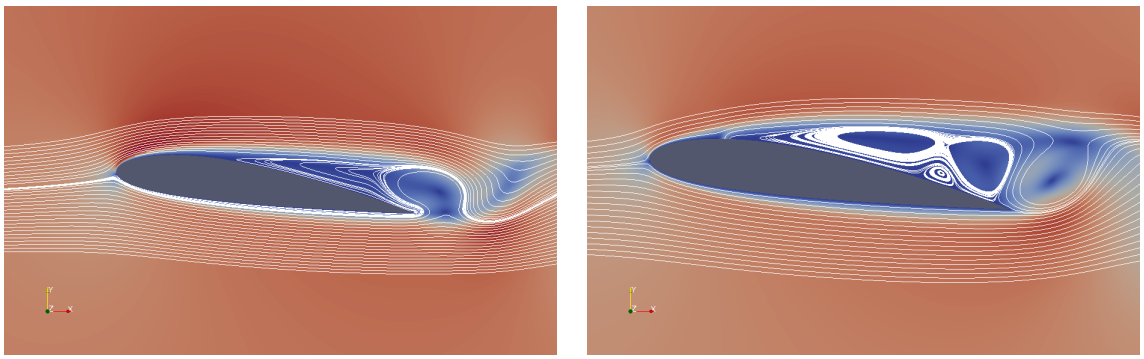

(a) Nominal case without synthetic jet implementation.

(b) Synthetic jet with an amplitude of 40%

Figure 4.19: Airfoil streamlines.

4.2.3. Viscous vs pressure drag

From Figure 4.17 we can deduce that overall drag is increased. Nevertheless, we want to analyze how each one increase respect the blowing amplitude.

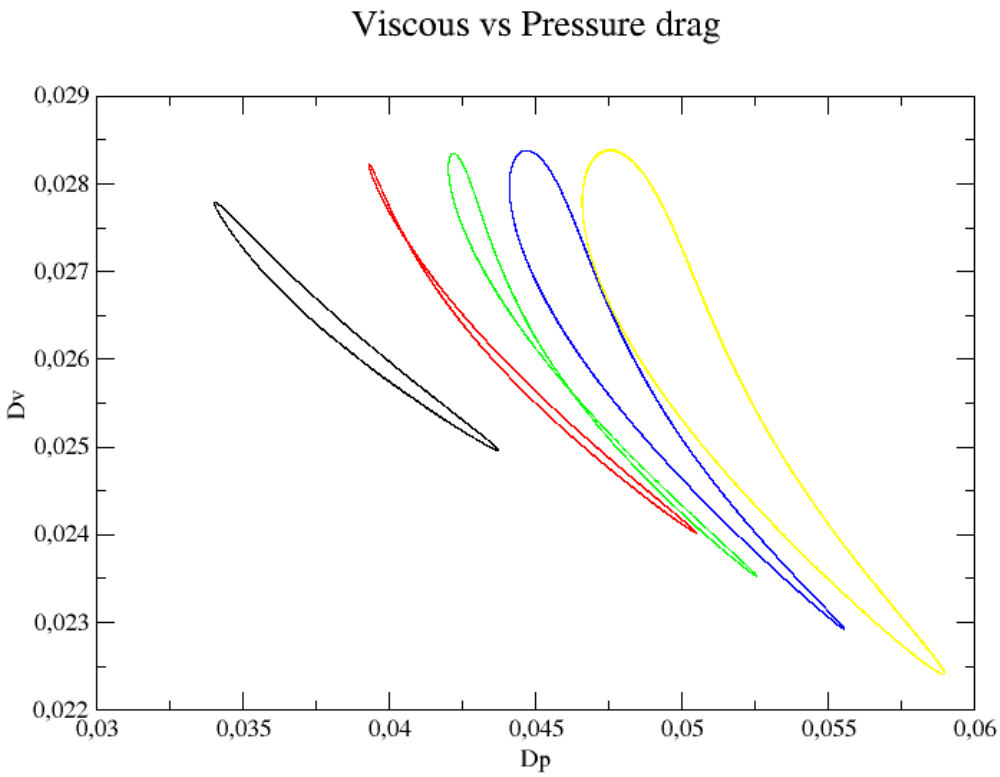

Figure 4.20: Viscous drag vs pressure drag for different suction amplitudes.

	D_V	D_P
0%	0.0263	0.0384
10%	0.0261	0.0440
20%	0.0259	0.0464
30%	0.0256	0.0491
40%	0.0254	0.0521

Table 4.8: Detailed results from viscous and pressure drag.

From Figure 4.20 and Table 4.8 we observe that viscous drag have small reduction due to the boundary layer moves forward to the leading edge and therefore less surfaces where the laminar boundary layer actuates. However, the pressure drag increases because separation occurs earlier and the wake is wider. In Figure 4.21 we can observe clearly how the two drags evolve with amplitude.

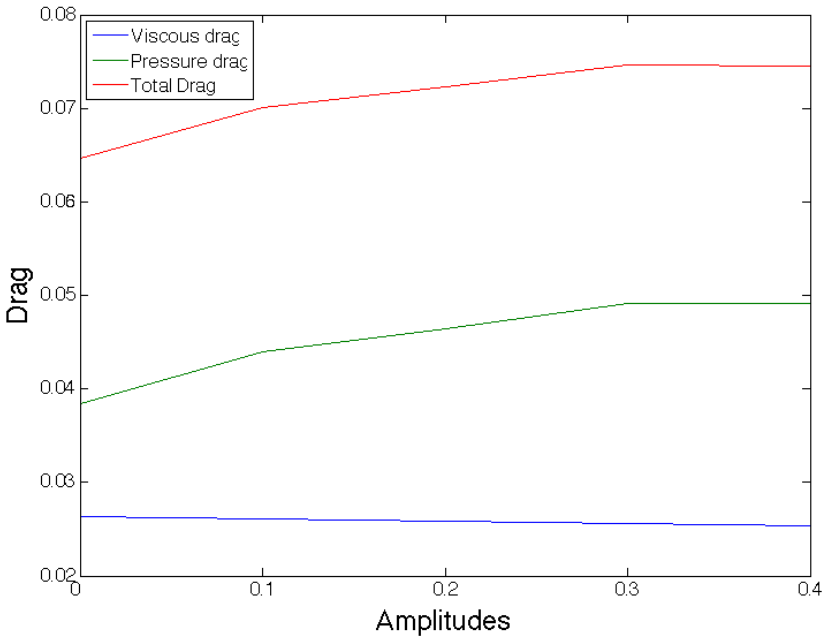

Figure 4.21: Viscous drag vs pressure drag for different suction amplitudes.

As we have said the viscous drag have a small evolution whereas the pressure drag have a huge increase.

4.2.4. Pressure distribution

Another fact where we can assess the decrease the aerodynamic performances is the pressure distribution (Figure 4.22)

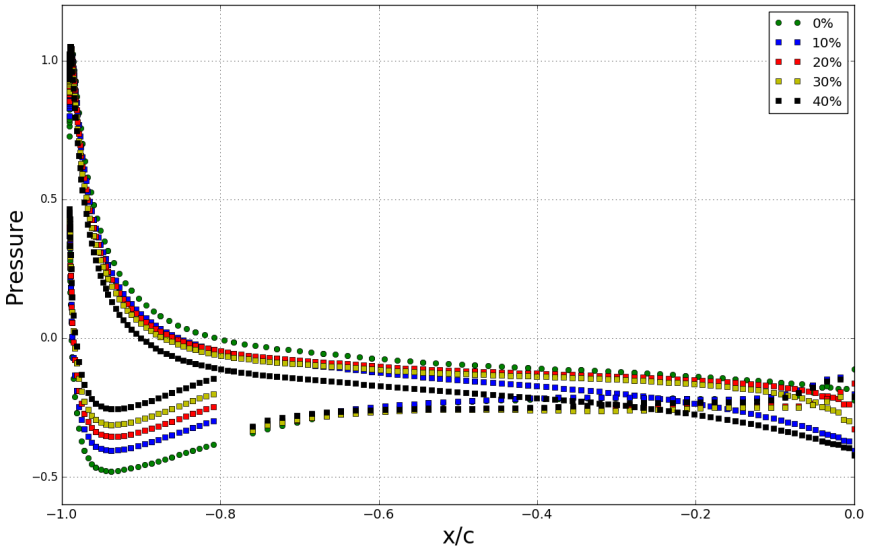

Figure 4.22: Pressure distribution for all amplitudes.

As we can observe, when the amplitude is increased the pressure difference between the upper and lower surfaces tends to reduce. We can also observe a sudden change on pressure before and after the jet slot. As we have said we attribute this changes to the fact that the gaussian is not a closed distribution where the domain is infinity.

4.2.5. Vortex shedding frequency

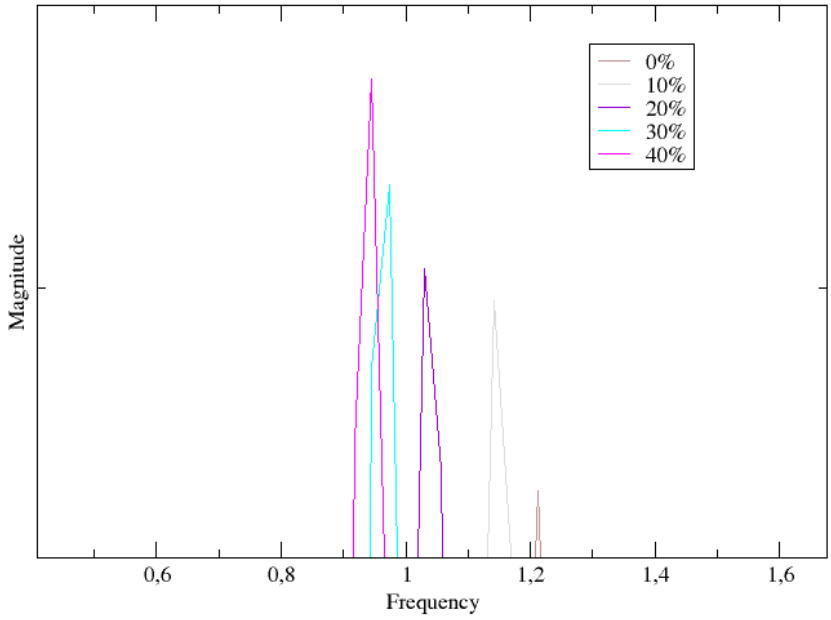

Figure 4.23: Vortex shedding first harmonic frequencies for different amplitudes.

With the fourier transform we can perform the frequencies spectrum for each amplitude. If we observe the peaks that are closer to the origin (first harmonics) they gives the vortex shedding frequencies that we can observe at Table 4.9.

As we can observe, instead of suction that the frequency tended to decrease in this type of excitation the frequency is increased. From Figure 4.24 we observe that vortex shedding amplitude increase.

	Frequency
0%	1.2120
-10%	1.1412
-20%	1.0305
-30%	0.9740
-40%	0.9462

Table 4.9: Vortex shedding frequencies.

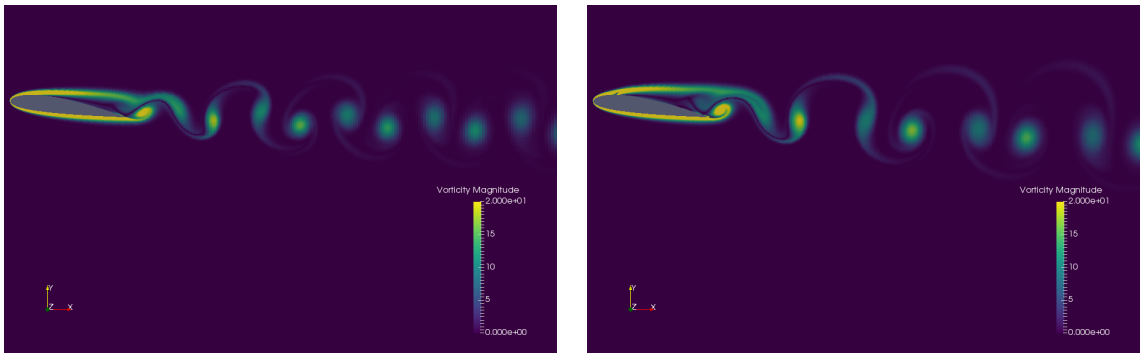

(a) Vortex shedding nominal case. (b) Vortex shedding for an amplitud of 40%.

Figure 4.24: Vorticity assessment.

4.2.6. Momentum coefficient

As the amplitude remains is not temporal dependent we can use the equation 4.19 to obtain the different momentum coefficients.

	C_μ
0%	0
10%	$1.8 \cdot 10^{-3}$
20%	$7.1 \cdot 10^{-3}$
30%	$1.6 \cdot 10^{-2}$
40%	$2.84 \cdot 10^{-2}$

Table 4.10: Momentum coefficient for the different amplitudes.

Note that the equation 4.19 only depends on the amplitude. For this reason, we obtain the same momentum coefficients for the different amplitudes as we can corroborate with Table 4.10.

4.3. Results comparison

Once we have all the desired continuous simulations performed. We compare both excitations to discuss the pros and cons of each type of excitation. To do this we put together all the results in the Table 4.11 and we assess the lift and drag coefficients for all the performed simulations in Figure 4.25.

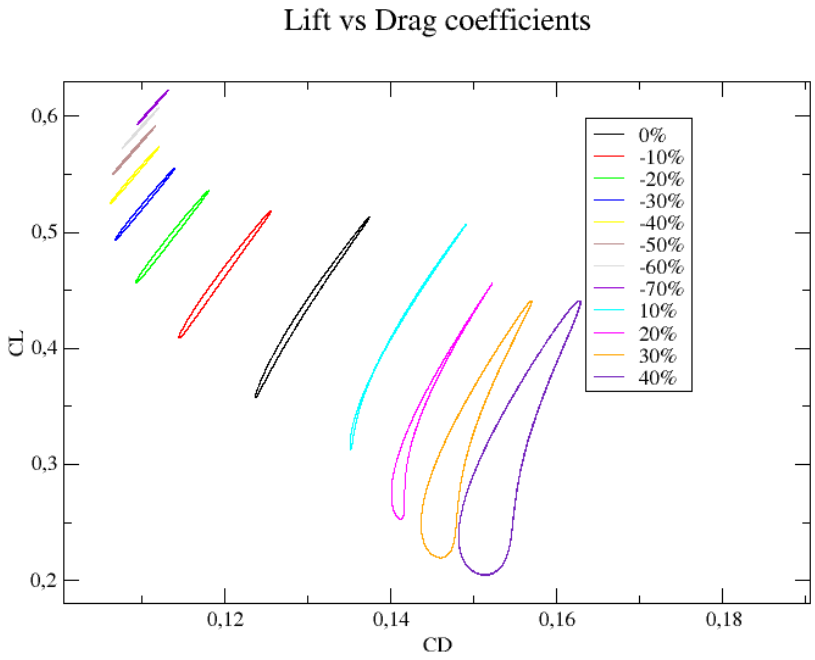

Figure 4.25: Lift and drag coefficients for each simulation.

		C_L	C_D	σ_L	σ_D	wss [L]	D_V	D_P	Frequency	e^2	C_μ
Suction	0%	0.4311	0.1297	0.0552	0.0049	0.3528	0.0263	0.0348	1.2120	3.3233	0
	-10%	0.4618	0.1196	0.0384	0.0039	0.4260	0.0272	0.0325	1.2935	3.8612	$1.8 \cdot 10^{-3}$
	-20%	0.4947	0.1134	0.0282	0.0031	0.4823	0.0287	0.0279	1.3464	4.3624	$7.1 \cdot 10^{-3}$
	-30%	0.5237	0.1102	0.02180	0.0025	0.5184	0.0306	0.0244	1.3967	4.7522	$1.6 \cdot 10^{-2}$
	-40%	0.5489	0.1090	0.0176	0.0021	0.5535	0.0327	0.0217	1.4503	5.0357	$2.84 \cdot 10^{-2}$
	-50%	0.5704	0.1089	0.0146	0.0018	0.5726	0.0350	0.0194	1.4754	5.2378	$4.43 \cdot 10^{-2}$
	-60%	0.5898	0.1097	0.0124	0.0015	0.5907	0.0373	0.0175	1.5034	5.3765	$6.38 \cdot 10^{-2}$
	-70%	0.6074	0.1112	0.0106	0.0013	0.6087	0.0389	0.0157	1.5287	5.4622	$8.68 \cdot 10^{-2}$
Blowing	10%	0.4004	0.1403	0.0691	0.0051	0.3155	0.0261	0.0440	1.1412	2.8538	$1.8 \cdot 10^{-3}$
	20%	0.3447	0.1447	0.0724	0.0042	0.2975	0.0259	0.0464	1.0305	2.3821	$7.1 \cdot 10^{-3}$
	30%	0.3199	0.1494	0.0791	0.0043	0.2773	0.0256	0.0491	0.9740	2.1412	$1.6 \cdot 10^{-2}$
	40%	0.3120	0.1550	0.0842	0.0047	0.2370	0.0254	0.0521	0.9462	2.0129	$2.84 \cdot 10^{-2}$

Table 4.11: Simulation results.

From Figure 4.25 we clearly see that the suction excitation improve the aerodynamic performance while the blowing excitation deteriorate it. Moreover, we can observe that from high blowing amplitudes to high suction amplitudes the oscillation is reduced considerably due to the separation of boundary layer occurs backwards to the trailing edge and the wake is more tight. Nevertheless, as the momentum coefficient depend directly on the square amplitude. This means that high amplitudes suppose a high cost to the system in terms of energy and therefore weight that could counteract all the improvements achieved.

To have a better perception of the data that contains the Table 4.11 we compute the trends of the main parameters.

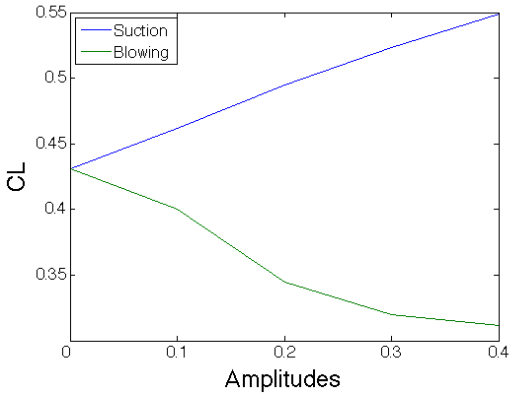

(a) Lift coefficient.

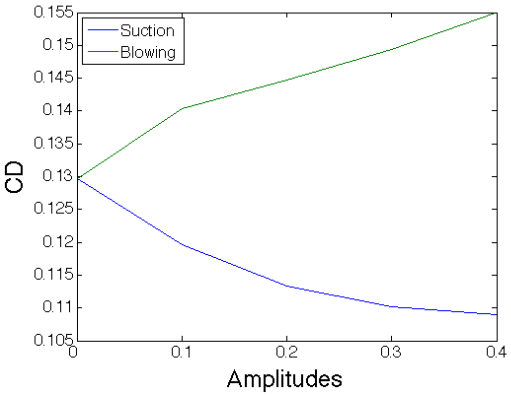

(b) Drag coefficient.

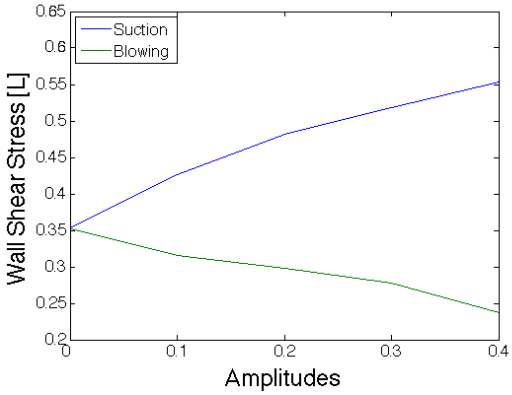

(c) Wall shear stress in terms of chord.

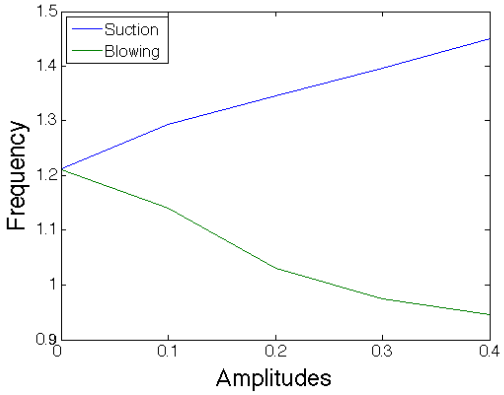

(d) Frequency.

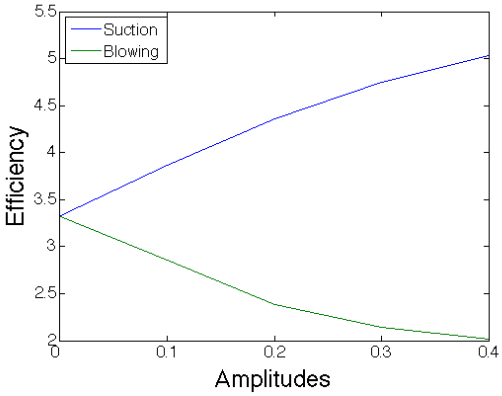

(e) Efficiency.

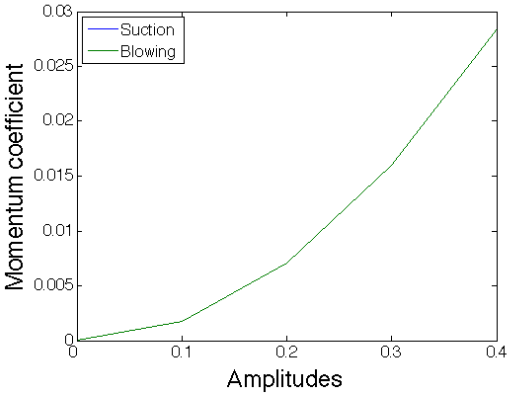

(f) Momentum coefficient.

Figure 4.26: Comparison of the main parameters for both suction and blowing excitations.

From Figure 4.26 we clearly observe the benefits of suction and the drawbacks of blowing. We extend the amplitudes until 40% for a better comparison between the excitations. The momentum coefficient graph both curves are the same because the equation only depends on the square amplitude.

4.4. Future work

To assess better the synthetic jet behavior we would have liked to simulate with periodic boundary conditions. It has not been possible due to a misunderstanding when the temporal dependency was defined at the jet boundary condition on the set up file. We had to define that we wanted a temporal dependency at the specified boundary condition but we do not did it. Therefore, all the results obtained the amplitude do not vary according the set up frequency and we obtained results with a fixed amplitude that did not change with time. In spite of, in this section we would like to define the simulations that we tried to have a better assessment of the synthetic jet.

Firstly, the zero-net-mass-flow excitation that combines both expulsion and suction. It adds and subtract momentum to the flow and we define as:

$$V(x,t) = A \cdot e^{\frac{-(x-\mu)^2}{2\sigma^2}} \cdot cos(2\pi f_v \cdot t) \tag{4.20}$$

Where:

- V is the velocity field
- f_v is the vortex shedding frequency

Secondly, the periodic blowing that combines zero and blowing amplitude:

$$V(x,t) = A + (A \cdot e^{\frac{-(x-\mu)^2}{2\sigma^2}} \cdot cos(2\pi f_v \cdot t)) \tag{4.21}$$

Note, that this equation the amplitude domain is zero and 2*A.

Thirdly, the periodic suction that combines zero and suction amplitude:

$$V(x,t) = -A + (A \cdot e^{\frac{-(x-\mu)^2}{2\sigma^2}} \cdot cos(2\pi f_v \cdot t)) \tag{4.22}$$

As the periodic blowing, the amplitude goes from zero to -2*A. However, we have to remark that the last two excitations (periodic blowing and suction) have a difficult implementation, especially the periodic suction. To understand better this type of excitation we perform an approximation with a cosine instead of a gaussian distribution (Figure 4.27).

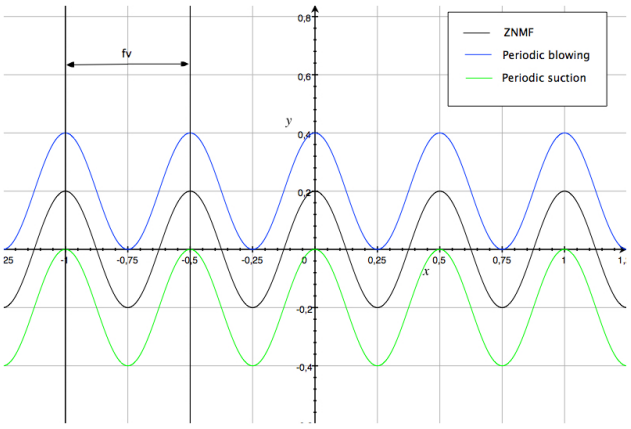

Figure 4.27: Periodic excitations on synthetic jet boundary condition.

CONCLUSIONS

The obtained outcomes focused on the main aim of this study that is to assess properly the best configuration for the synthetic jet that provides an improvement of the aerodynamic performances without forgetting the existent trade-off with the momentum coefficient allows us to accomplish the study goal.

With the results we conclude that the best excitation that provides a good performance to the flow is the suction. As we have seen, incrementing the suction amplitude the lift coefficient is increased whereas the drag coefficient is reduced and therefore the airfoil's efficiency increase in a way that almost doubles the nominal (without jet implementation) efficiency. However, this good results involve an increase of the momentum coefficient that suppose more energy into the system since more flux momentum has to be subtracted and surely more weight that could countereact the suction excitation benefits. Nevertheless, the study of synthetic jet system is out of our range and we could not assess properly the airfoil drawbacks that could suppose to increase the suction amplitude.

Moreover, moving the jet slot location closer to the boundary layer separation points seems to have a little positive change on the airfoil's performance. Even so, to optimize this type of excitation we should test the suction in other locations of the upper surface such as after the boundary layer to come up with a better configuration.

Also, the blowing excitation has been tested. However, we have seen a deterioration on the airfoil's performances. In spite of, we do not have to dismiss this excitation. It is true that for a jet location of 0.2L the suction behaves better than blowing. But, as we said above to have a complete evaluation we should change the jet slot location to observe the behavior of the airfoil.

The synthetic jet system entails an enormous range of possible configurations and it is difficult to come up with one an unique solution. Despite, this study lacks of the periodic boundary conditions. We have try to test this excitations but we did not obtain the expected outcomes. For this reason, to deal with more possible improvements on the airfoil it should be good to test this periodic excitations.

In order to test and extract the results that is the most significant part we should pay heed to all the intricate process that comes before the results and discussion. We would like to remark that this study has a practical purpose for the unmanned aerial vehicle Skywalker x6 and with more time it should be good to implement the synthetic jet with the suction boundary condition to evaluate how it behaves in the real world. Also, we would like to emphasis the developed algorithm to discretize with high accuracy the synthetic jet domain.

To conclude, we would like to remark the potential obtained benefits with the suction excitation. But, as the jet synthetic depends on numerous parameters, several simulations with multiple boundary conditions have to be done in order to assess with more accuracy this system because this device could involve achievements on the aerospace industry in the near future.

BIBLIOGRAPHY

[1] Mark A.Feero, Philippe Lavoie and Pierre E.Sullivan. “Influence of synthetic jet location on active control of an airfoil at low Reynolds number”. (July 7, 2017) 1

[2] Xu Xiaoping, Zhou Zhou and Wang Rui “Numerical Investigations of Synthetic Jet Control for TAU0015 Airfoil”. (June 4, 2014) 1, 24

[3] M. Moshfeghi and N. Hur “Numerical study on the effects of a synthetic jet actuator on S809 airfoil aerodynamics at different flow regimes and jet flow angles”. (October 26, 2016) 1

[4] Mark A. Feero, Sebastian D. Goodfellow, Philippe Lavoie, and Pierre E. Sullivan “Flow Reattachment Using Synthetic Jet Actuation on a Low-Reynolds-Number Airfoil”. 1, 24

[5] Web application: Calculadora de profundidad de campo (PDC) 4

[6] “The NACA airfoils”. *Geometry for Aerodynamicists*. (10/23/97):1–4 7

[7] Cristophe Geuzaine and Jean-François Remacle. “Gmsh”. *Gmsh Reference Manual*. (September 6, 2017):1–69 9, 11, 13

[8] Department of Aeronautics, Imperial College London, UK and Scientific Computing and Imaging Institute, University of Utah, USA “Incompressible Navier-Stokes Solver”. *Nektar++: Spectral/hp Element Framework*. (Version 4.4.0, March 8, 2017): 133–145. 15, 16, 18

[9] Sebastian D. Goodfellow, Serhiy Yarusevych and Pierre E.Sullivan. “Momentum coefficient as a parameter for aerodynamic flow control with synthetic jets”. 24

[10] Hoonil Park, Jun-Ho Cho, Joonho Lee, Dong-Ho Lee and Kyu Hong Kim “Experimental study on synthetic jet array for aerodynamic drag reduction of a simplified car”. (July 22, 2013) 24

APPENDICES

APPENDIX A. PHOTOGRAMMETRY

A.1. Photos alignment parameters

When the alignment of the photos and the dense cloud of points are done Agisoft Photoscan generates a report that contains all the camara parameters, alignment errors, digital elevation model, etc.

Report2

Informe de pre-procesamiento

06 June 2017

Survey Data

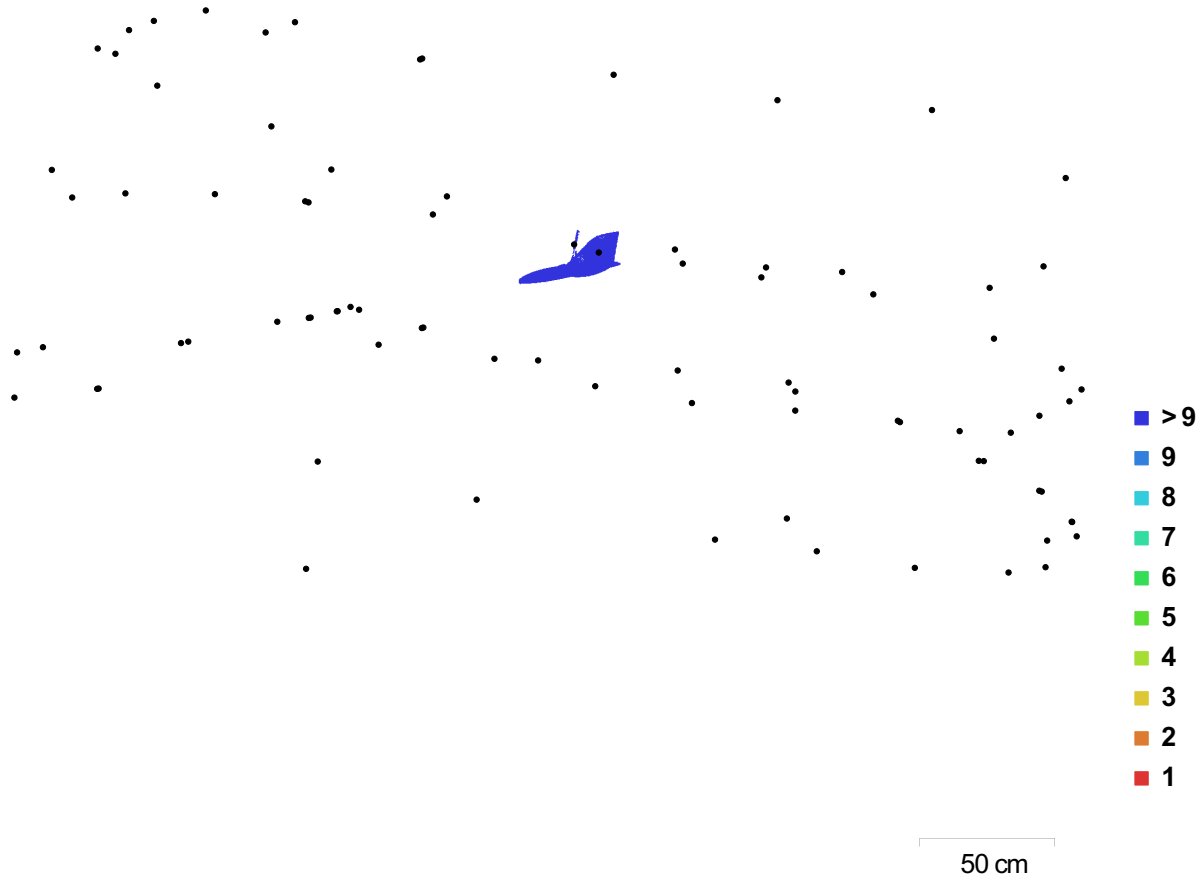

Fig. 1. Camera locations and image overlap.

Number of images:	86	Camera stations:	85
Flying altitude:	1.67 m	Tie points:	8,184
Ground resolution:	0.162 mm/pix	Projections:	18,911
Coverage area:	299 cm²	Reprojection error:	4.91 pix

Camera Model	Resolution	Focal Length	Pixel Size	Precalibrated
NIKON D7000 (50 mm)	4928 x 3264	50 mm	4.88 x 4.88 µm	No

Table 1. Cameras.

Camera Calibration

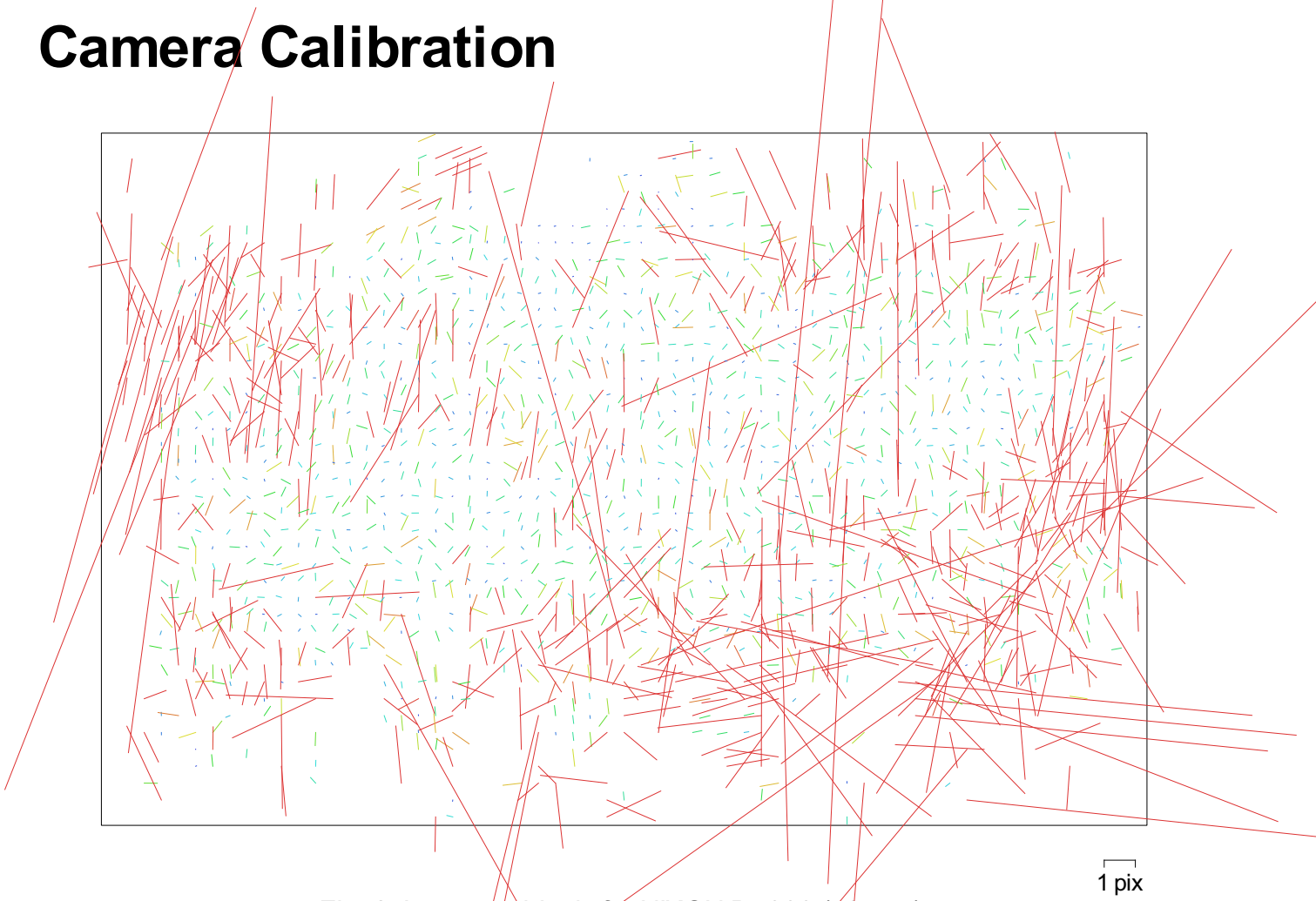

Fig. 2. Image residuals for NIKON D7000 (50 mm).

NIKON D7000 (50 mm)

86 images

Resolution	Focal Length	Pixel Size	Precalibrated
4928 x 3264	**50 mm**	**4.88 x 4.88 µm**	**No**

Type:	Frame	F:	11144.6
Cx:	-84.694	B1:	4.48499
Cy:	173.372	B2:	13.0771
K1:	-0.12241	P1:	-0.00227648
K2:	5.22671	P2:	0.00805638
K3:	-117.028	P3:	-21.908
K4:	1022.47	P4:	231.539

Ground Control Points

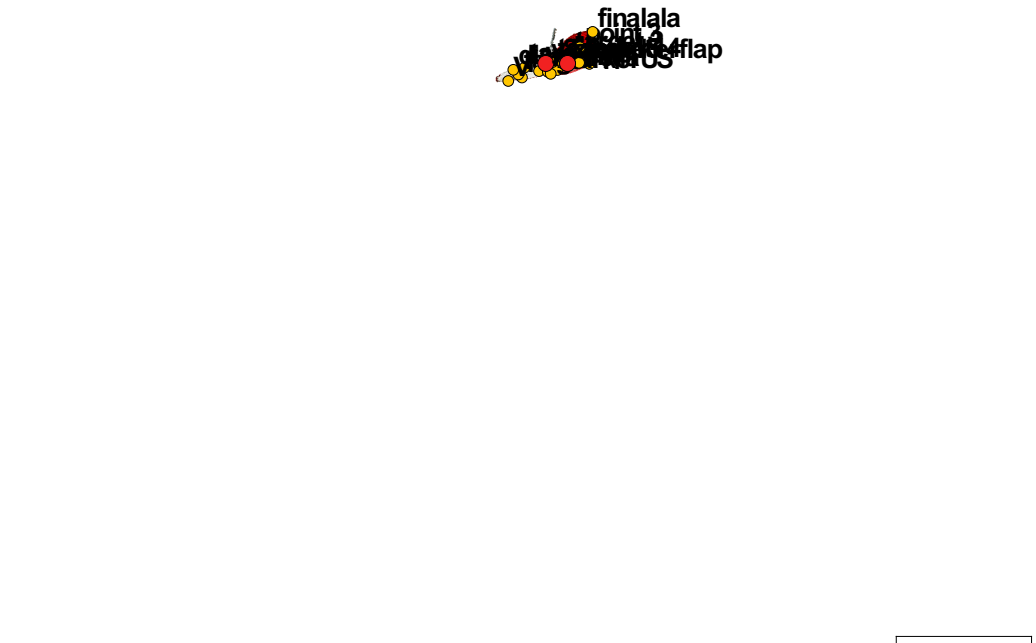

Fig. 3. GCP locations.

Count	X error (mm)	Y error (mm)	Z error (mm)	XY error (mm)	Total (mm)	Image (pix)
3	0.133145	0.210939	1.43219e-05	0.249445	0.249445	0.377

Table 2. Control points RMSE.

Label	X error (mm)	Y error (mm)	Z error (mm)	Total (mm)	Image (pix)
y8	0.187478	0.107206	1.3212e-05	0.215966	0.441 (8)
x8	-0.108889	0.187517	2.05063e-05	0.21684	0.243 (8)
center	-0.0786001	-0.294668	-4.50432e-06	0.304971	0.400 (13)
Total	**0.133145**	**0.210939**	**1.43219e-05**	**0.249445**	**0.377**

Table 3. Control points.

Label	X error (mm)	Y error (mm)	Z error (mm)	Total (mm)	Image (pix)
H					0.899 (35)
point 1					0.196 (11)
target 2					0.740 (22)
target 4					0.532 (19)
target 15					0.435 (16)
target 17					0.485 (30)
markerflap					0.440 (34)
brut					0.519 (14)
diana1					0.511 (21)
estrella					0.856 (33)
markerUS					0.530 (28)
T					0.699 (17)
target14					0.577 (15)
V					0.634 (27)
point 3					0.679 (10)
finalala					0.410 (18)
Total					

Table 4. Check points.

Scale Bars

Label	Distance (m)	Error (m)
x8_center	0.0799712	-2.88353e-05
y8_center	0.0804023	0.000402315
y8_x8	0.112871	-0.000266163
Total		**0.000279005**

Table 5. Control scale bars.

Digital Elevation Model

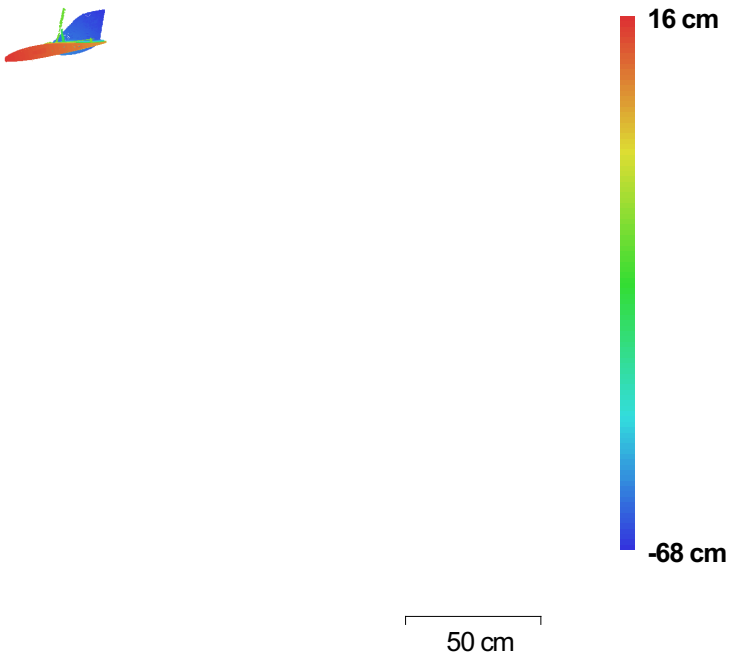

Fig. 4. Reconstructed digital elevation model.

Resolution:	unknown
Point density:	unknown

Processing Parameters

General	
Cameras	86
Aligned cameras	85
Markers	20
Scale bars	3
Coordinate system	Local Coordinates (m)
Point Cloud	
Points	8,184 of 14,574
RMS reprojection error	0.922887 (4.90563 pix)
Max reprojection error	53.8584 (226.319 pix)
Mean key point size	8.66819 pix
Effective overlap	2.47681
Alignment parameters	
Accuracy	Medium
Pair preselection	Generic
Key point limit	40,000
Tie point limit	4,000
Constrain features by mask	Yes
Adaptive camera model fitting	Yes
Matching time	2 minutes 11 seconds
Alignment time	0 seconds
Optimization parameters	
Parameters	f, b1, b2, cx, cy, k1-k4, p1-p4
Optimization time	1 seconds
Dense Point Cloud	
Points	5,322,435
Reconstruction parameters	
Quality	High
Depth filtering	Mild
Depth maps generation time	31 minutes 19 seconds
Dense cloud generation time	3 minutes 30 seconds
Software	
Version	1.2.6 build 2834
Platform	Windows 64 bit

A.2. Airfoil photos

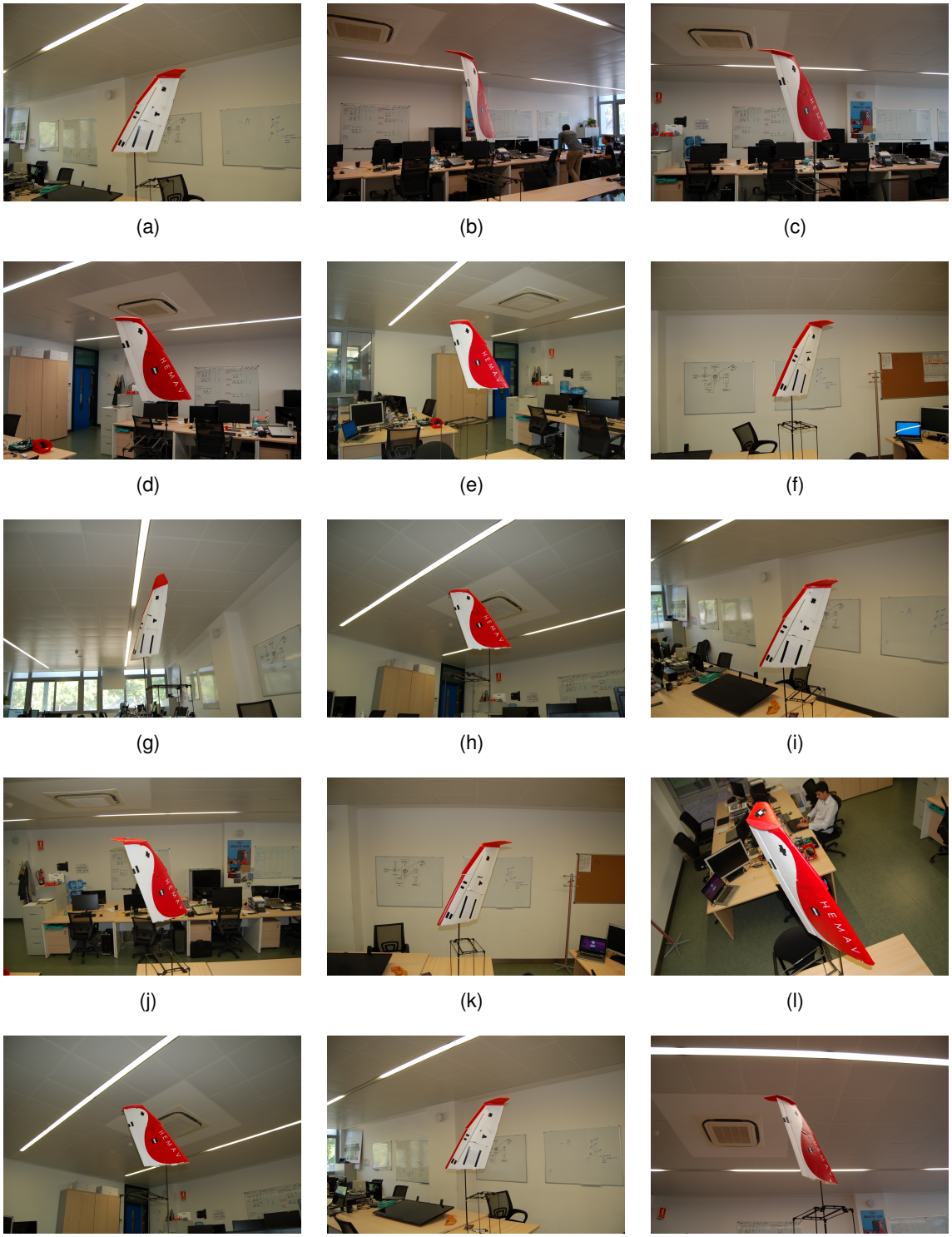

(a) (b) (c)

(d) (e) (f)

(g) (h) (i)

(j) (k) (l)

(m) (n) (o)

Figure A.1: Skywalker x6 airfoil photos

APPENDIX B. MESH

Below we can find the detailed code used to perform the mesh adaptation for the synthetic jet. First of all we have to divide the airfoil's upper surface on the three separations that we have discussed on section 2.2..

```
//jetposition
If (jetyes==1)

  yt = 5*t*c*(a0*Sqrt(jsl/c)+a1*(jsl/c)+a2*(jsl/c)^2+a3*(jsl/c)^3+a4*(jsl/c)^4);
  If (jsl != 0)
    dytdx = 5*t*(a0/(2*Sqrt(jsl/c))+a1+2*a2*(jsl/c)+3*a3*(jsl/c)^2+4*a4*(jsl/c)^3);
  EndIf
  If (jsl <= p) // camber for x/c <= p
    yc = m*(jsl/p^2)*(2*p-jsl/c);
    dycdx = (2*m/p^2)*(p-jsl/c);
    Else // camber for x/c > p
    yc = m*((c-jsl)/(1-p)^2)*(1+jsl/c-2*p);
    dycdx = (2*m/(1-p)^2)*(p-jsl/c);
  EndIf
  th = Atan(dycdx);
  xu0 = -c+jsl-yt*Sin(th);
  yu0 = yc+yt*Cos(th);
  xl0 = -c+jsl+yt*Sin(th);
  yl0 = yc-yt*Cos(th);
  xujet = xte+(xu0-xte)*Cos(aoa)+(yu0-yte)*Sin(aoa);
  yujet = yte-(xu0-xte)*Sin(aoa)+(yu0-yte)*Cos(aoa);
jetp=newp;
Point(jetp)={xujet,yujet,0};
//jetposition1
xv=jsl;
n=0;
limit=5000;
For n In {0:limit}
  yt = 5*t*c*(a0*Sqrt(xv/c)+a1*(xv/c)+a2*(xv/c)^2+a3*(xv/c)^3+a4*(xv/c)^4);
  If (xv != 0)
    dytdx = 5*t*(a0/(2*Sqrt(xv/c))+a1+2*a2*(xv/c)+3*a3*(xv/c)^2+4*a4*(xv/c)^3);
  EndIf
  If (xv <= p) // camber for x/c <= p
    yc = m*(xv/p^2)*(2*p-xv/c);
    dycdx = (2*m/p^2)*(p-xv/c);
    Else // camber for x/c > p
    yc = m*((c-xv)/(1-p)^2)*(1+xv/c-2*p);
    dycdx = (2*m/(1-p)^2)*(p-xv/c);
  EndIf
  th = Atan(dycdx);
  xu0 = -c+xv-yt*Sin(th);
  yu0 = yc+yt*Cos(th);
  xl0 = -c+xv+yt*Sin(th);
  yl0 = yc-yt*Cos(th);
  xuj1 = xte+(xu0-xte)*Cos(aoa)+(yu0-yte)*Sin(aoa);
  yuj1 = yte-(xu0-xte)*Sin(aoa)+(yu0-yte)*Cos(aoa);
  d=Sqrt((xuj1-xujet)^2+(yuj1-yujet)^2);
  //Printf('distance=%g',d);
  If (d<=jst/2)
  xujet1=xuj1;
  yujet1=yuj1;
  Else
  n=limit+1;
  EndIf
xv=xv+0.001;
EndFor
```

ActionScript Tab Width: 8 Ln 1729

(a) Central and forward points.

```
//jetposition2
xv=jsl;
n=0;
For n In {0:limit}
  yt = 5*t*c*(a0*Sqrt(xv/c)+a1*(xv/c)+a2*(xv/c)^2+a3*(xv/c)^3+a4*(xv/c)^4);
  If (xv != 0)
    dytdx = 5*t*(a0/(2*Sqrt(xv/c))+a1+2*a2*(xv/c)+3*a3*(xv/c)^2+4*a4*(xv/c)^3);
  EndIf
  If (xv <= p) // camber for x/c <= p
    yc = m*(xv/p^2)*(2*p-xv/c);
    dycdx = (2*m/p^2)*(p-xv/c);
    Else // camber for x/c > p
    yc = m*((c-xv)/(1-p)^2)*(1+xv/c-2*p);
    dycdx = (2*m/(1-p)^2)*(p-xv/c);
  EndIf
  th = Atan(dycdx);
  xu0 = -c+xv-yt*Sin(th);
  yu0 = yc+yt*Cos(th);
  xl0 = -c+xv+yt*Sin(th);
  yl0 = yc-yt*Cos(th);
  xuj2 = xte+(xu0-xte)*Cos(aoa)+(yu0-yte)*Sin(aoa);
  yuj2 = yte-(xu0-xte)*Sin(aoa)+(yu0-yte)*Cos(aoa);
  d=Sqrt((xuj2-xujet)^2+(yuj2-yujet)^2);
  //Printf('distance=%g',d);
  If (d<=jst/2)
  xujet2=xuj2;
  yujet2=yuj2;
  Else
  n=limit+1;
  EndIf
xv=xv-0.0001;
EndFor
jet2p=newp;
Point(jet2p)={xujet2,yujet2,0};
EndIf
```

(b) Backward points.

Figure B.1: Straight line boundaries that define the synthetic jet active domain.

As we can observer from Figure B.1 the first step is to define the jet central point that is an input for the user. Then, following the NACA equations we compute the points with a high accuracy around this central points and we fix the points that accomplish the distance criteria. Once this is done then we are able to join the points with lines thinking in the desired divisions (Figure B.2).

```
//NACA AIRFOIL DEFINITION
xp=1.1*c; iL=-1; iU=-1;
encontrado=0;
For i In {0 : N-1}

  //* chord line definition
  xc = c*(1+Cos((i*Pi)/N))/2;
  //Printf('%g %g %g %g',xc,pj*c,xp,pj*c);
  If ((xc < pj*c) && (xp >= pj*c))
    xj = pj*c; // relocate point on jet position
    ij = i; // save jet position index
  EndIf
  x[i] = xc; // store point
  xp = x[i];

    //* thickness (symmetric airfoil)
  yta = 5*t*c*(a0*Sqrt(x[i]/c)+a1*(x[i]/c)+a2*(x[i]/c)^2+a3*(x[i]/c)^3+a4*(x[i]/c)^4);
  If (x[i] != 0)
    dytdxa[i] = 5*t*(a0/(2*Sqrt(x[i]/c))+a1+2*a2*(x[i]/c)+3*a3*(x[i]/c)^2+4*a4*(x[i]/c)^3);
  EndIf

  //* camber
  If (x[i] <= p) // camber for x/c <= p
    yc = m*(x[i]/p^2)*(2*p-x[i]/c);
    dycdxa[i] = (2*m/p^2)*(p-x[i]/c);
    Else
    yc = m*((c-x[i])/(1-p)^2)*(1+x[i]/c-2*p);
    dycdxa[i] = (2*m/(1-p)^2)*(p-x[i]/c);
  EndIf

  //* airfoil (x,y) coordinates (origin at trailing edege)
  th = Atan(dycdxa[i]);
  xu0 = -c+x[i]-yta*Sin(th);
  yu0 = yc+yta*Cos(th);
  xl0 = -c+x[i]+yta*Sin(th);
  yl0 = yc-yta*Cos(th);
  xu[i] = xte+(xu0-xte)*Cos(aoa)+(yu0-yte)*Sin(aoa);
  yu[i] = yte-(xu0-xte)*Sin(aoa)+(yu0-yte)*Cos(aoa);
  xl[i] = xte+(xl0-xte)*Cos(aoa)+(yl0-yte)*Sin(aoa);
  yl[i] = yte-(xl0-xte)*Sin(aoa)+(yl0-yte)*Cos(aoa);
  //Printf('%g',xu[i]);
  //* generate points
  iL = iL+1; lsP[iL] = newp; Point(lsP[iL]) = {xl[i],yl[i],0};
  iU=iU+1; usP[iU] = newp; Point(usP[iU]) = {xu[i], yu[i], 0, ls};
```

(a) NACA equations to compute the airfoil points.

```
If (jetyes==1)
  If (xu[i] > xujet1)
  stop1=iU;
  EndIf
  If ((xu[i] < xujet2)&&(encontrado==0))
  stop2=iU;
  encontrado=1;
  EndIf
  If (xu[i]>xuj)
  stop3=iU;
  EndIf
EndIf

EndFor
If (jetyes==1)
  jetbL=newl; Spline(jetbL) = {teP,usP[{1:stop1}],jet1p};
  jetL=newl; Line(jetL) = {jet1p,jet2p};
  jetfL=newl; Spline(jetfL) = {jet2p,usP[{stop2:stop3}],ujP};
  ufsL = newl; Spline(ufsL) = {ujP,usP[{stop3+1:#usP[]-1}],leP};
Else
  uasL = newl; Spline(uasL) = {teP,usP[{1:ij-1}],ujP};
  ufsL = newl; Spline(ufsL) = {ujP,usP[{ij:#usP[]-1}],leP};
EndIf

lasL = newl; Spline(lasL) = {teP,lsP[{1:ij-1}],ljP};
lfsL = newl; Spline(lfsL) = {ljP,lsP[{ij:#lsP[]-1}],leP};
```

(b) Points union.

Figure B.2: Airfoil lines definition.

The next step is to create and extend the jet lines until the boundaries. For this reason, we build two lines parallels to the lines next to each one until they intersect with the next surface (mid field).

```
//jet1 intersections
If (jetyes==1)

mn1=(yunf-yutenf)/(xunf-xutenf);
nn1=yunf-(mn1*xunf);
mn2=(yutenf-yte)/(xutenf-xte);
nn2=yujet1-(mn2*xujet1);
xin1=(nn2-nn1)/(mn1-mn2);
yin1=(mn1*xin1)+nn1;
injetn1=newp; Point(injetn1)={xin1,yin1,0};
injetn1l=newl; Line(injetn1l)={jet1p,injetn1};

//jet2 intersections
//circle intersec
delta=0;
mn3=(yujnf-yuj)/(xujnf-xuj)-0.8;
nn3=yujet2-(mn3*xujet2);
radi=Sqrt((yujnf-ycnf)^2+(xujnf-xcnf)^2);
a3=(mn3)^2+1;
b3=(2*(nn3-ycnf)*mn3)-(2*xcnf);
c3=(xcnf)^2+(nn3-ycnf)^2-(radi)^2;
xin2=(-b3+Sqrt((b3^2)-(4*a3*c3)))/(2*a3);
xin3=(-b3-Sqrt((b3^2)-(4*a3*c3)))/(2*a3);
yin2=(mn3*xin2)+nn3;
yin3=(mn3*xin3)+nn3;
dinter1=Sqrt((xin2-xunf)^2+(yin2-yunf)^2);
dinter2=Sqrt((xin3-xunf)^2+(yin3-yunf)^2);
If (dinter1<dinter2) //Equation with 2 solution. 1 have to be the correct
xinc=xin2;
yinc=yin2;
Else
xinc=xin3;
yinc=yin3;
EndIf
// Line intersection
xin4=(nn3-nn1)/(mn1-mn3);
yin4=(mn1*xin4)+nn1;
//Choice betwwen circle or line intersect
If (xin4 < xunf)
xninj2=xinc;
yninj2=yinc;
Else
xninj2=xin4;
yninj2=yin4;
delta=1;
EndIf
injetn2=newp; Point(injetn2)={xninj2,yninj2,0};
injetn2l=newl; Line(injetn2l)={jet2p,injetn2};
```

(a) Intersection with upper line and circle.

```
//Choice betwwen circle or line intersect
If (xin4 < xunf)
xninj2=xinc;
yninj2=yinc;
Else
xninj2=xin4;
yninj2=yin4;
delta=1;
EndIf
injetn2=newp; Point(injetn2)={xninj2,yninj2,0};
injetn2l=newl; Line(injetn2l)={jet2p,injetn2};

//compound line have a bad behaviour we use spline
If(delta==1)
xcpoint1=((xujnf-xunf)/2)+xunf;
ycpoint1=ycnf+Sqrt((radi)^2-(xcpoint1-xcnf)^2);
controlP1=newp;
Point(controlP1)={xcpoint1,ycpoint1,0};
EndIf
EndIf

If (jetyes==1)
//jetnL1=newl; Circle(jetnL1) = {injetn2,cnfP,unfP};
//jetnL2=newl; Line(jetnL2) = {unfP,injetn1};
//jetnLu=newl; Compound Line(jetnLu)={jetnL1,jetnL2};
  If (delta==1)
    jetn2L=newl; Spline(jetn2L) = {ujnfP,controlP1,unfP,injetn2};
    jetnLu=newl; Line(jetnLu) = {injetn2,injetn1};
  Else
    jetn2L=newl; Circle(jetn2L) = {ujnfP,cnfP,injetn2};
    jetnLu=newl; Spline(jetnLu) = {injetn2,unfP,injetn1};
  EndIf

  jetn1L=newl; Line(jetn1L) = {injetn1,utenfP};
Else
  uanfL1=newl; Circle(uanfL1) = {ujnfP,cnfP,unfP};
  uanfL2=newl; Line(uanfL2) = {unfP,utenfP};
  uanfL=newl; Compound Line(uanfL)={uanfL1,uanfL2};
EndIf
```

(b) Election between line or circle and then join the points with lines.

Figure B.3: Intersection with mid field boundary.

The code from Figure B.3 is repeated two times more for the mid and far field only changing certain aspects. Once all the intersections and lines are computed. We have to redefine the existing line loops and create the new ones (Figure B.4).

```
// Jet line loop implementation
If (jetyes==1)
  jetnLl = newll; Line Loop(jetnLl) = {injetn2l, jetnLu, -injetn1l, jetL};
  jetn2Ll = newll; Line Loop(jetn2Ll) = {ujnfL, jetn2L, -injetn2l, jetfL};
  jetn1Ll = newll; Line Loop(jetn1Ll) = {injetn1l, jetn1L, -utenfL, jetbL};

  jetmLl = newll; Line Loop(jetmLl) = {injetm2l, jetmL, -injetm1l, -jetnLu};
  jetm2Ll = newll; Line Loop(jetm2Ll) = {ujmfL, jetm2L, -injetm2l, -jetn2L};
  jetm1Ll = newll; Line Loop(jetm1Ll) = {injetm1l, jetm1L, -utemfL, -jetn1L};

  jetfLl = newll; Line Loop(jetfLl) = {injetf2l, jetffL, -injetf1l, -jetmL};
  jetf2Ll = newll; Line Loop(jetf2Ll) = {ujffL, jetf2L, -injetf2l, -jetm2L};
  jetf1Ll = newll; Line Loop(jetf1Ll) = {injetf1l, jetf1L, -uteffL, -jetm1L};


Else
  uanfLl = newll; Line Loop(uanfLl) = {ujnfL, uanfL, -utenfL, uasL};
  uamfLl = newll; Line Loop(uamfLl) = {ujmfL, uamfL, -utemfL, -uanfL};
  uaffLl = newll; Line Loop(uaffLl) = {ujffL, uaffL, -uteffL, -uamfL};
EndIf
```

Figure B.4: New and redefined line loops.

Next step is to apply the transfinite algorithm to each line as we can observe in Figure B.5.

```
If (jetyes==1)
Transfinite Line {jetn2L} = tn2 Using Progression pn2;
Transfinite Line {jetnLu} = tn Using Progression pn;
Transfinite Line {jetn1L} = tn1 Using Progression pn1;
Transfinite Line {jetbL} = tn1 Using Progression pbL;
Transfinite Line {jetL} = tn Using Progression pL;
Transfinite Line {jetfL} = tn2 Using Progression pfL;
Transfinite Line {injetn2l} = Nnf Using Progression Kujnf;
Transfinite Line {injetn1l} = Nnf Using Progression Kujnf;

Transfinite Line {injetm2l} = Nmf Using Progression Kujmf;
Transfinite Line {injetm1l} = Nmf Using Progression Kujmf;
Transfinite Line {jetm2L} = tn2 Using Progression 1;
Transfinite Line {jetmL} =tn Using Progression 1.01;
Transfinite Line {jetm1L} = tn1 Using Progression 1;

Transfinite Line {jetf2L} = tn2 Using Progression 1;
Transfinite Line {jetffL} =tn Using Progression 1;
Transfinite Line {jetf1L} = tn1 Using Progression 1;
Transfinite Line {injetf2l} = Nff Using Progression Kujff;
Transfinite Line {injetf1l} = Nff Using Progression Kujff;

EndIf
```

Figure B.5: Transfinite algorithm for each line loop line.

On the transfinite algorithm before the progression we define the number of division of each line and then the separation between divisions. The final step is to compute the new and redefined surfaces and choose the physical surfaces that will set up our domain and where we can define the expansions (Figure B.6).

```
//jet surface
If (jetyes==1)
  jetn2S = news; Plane Surface(jetn2S) = {jetn2Ll};
  jetnS = news; Plane Surface(jetnS) = {jetnLl};
  jetn1S = news; Plane Surface(jetn1S) = {jetn1Ll};

  jetm2S = news; Plane Surface(jetm2S) = {jetm2Ll};
  jetmS = news; Plane Surface(jetmS) = {jetmLl};
  jetm1S = news; Plane Surface(jetm1S) = {jetm1Ll};

  jetf2S = news; Plane Surface(jetf2S) = {jetf2Ll};
  jetfS = news; Plane Surface(jetfS) = {jetfLl};
  jetf1S = news; Plane Surface(jetf1S) = {jetf1Ll};

  Transfinite Surface {jetn2S,jetnS,jetn1S,jetm2S,jetmS,jetm1S,jetf2S,jetfS,jetf1S};
  Recombine Surface {jetn2S,jetnS,jetn1S,jetm2S,jetmS,jetm1S,jetf2S,jetfS,jetf1S};
Else
  uanfS = news; Plane Surface(uanfS) = {uanfLl};
  uamfS = news; Plane Surface(uamfS) = {uamfLl};
  uaffS = news; Plane Surface(uaffS) = {uaffLl};
  Transfinite Surface {uanfS,uamfS,uaffS};
  Recombine Surface {uanfS,uamfS,uaffS};
EndIf
```

(a) New surfaces.

```
If (jetyes==1)
Color Red{Physical Line("Inlet") = {ufffL,jetf2L,jetffL,jetf1L,lfffL,laffL};}
Physical Line("AirfoilUS") = {jetbL,jetfL,ufsL};
Physical Line("Jetline") = {jetL};
Physical Surface("JetSurface") = {jetnS};
Physical Surface("UpperNearField") = {jetn2S,jetn1S,ufnfS};
Physical Surface("MidFieldExceptUpperWake") =
{ulmfS,jetm2S,jetmS,jetm1S,ufmfS,llmfS,lwmfS,lamfS,lfmfS};
Physical Surface("FarField") = {ulfffS,uwffS,jetf2S,jetfS,jetf1S,ufffS,llffS,lwffS,laffS,lfffS};

Else
Color Red{Physical Line("Inlet") = {ufffL,uaffL,lfffL,laffL};}
Physical Line("AirfoilUS") = {uasL,ufsL};
Physical Surface("UpperNearField") = {uanfS,ufnfS};
Physical Surface("MidFieldExceptUpperWake") = {ulmfS,uamfS,ufmfS,llmfS,lwmfS,lamfS,lfmfS};
Physical Surface("FarField") = {ulfffS,uwffS,uaffS,ufffS,llffS,lwffS,laffS,lfffS};
EndIf
```

(b) Physical surfaces.

Figure B.6: Creation of new surfaces and definition of physical surfaces.

APPENDIX C. RESULTS AND DISCUSSION

C.1. Convergence analysis

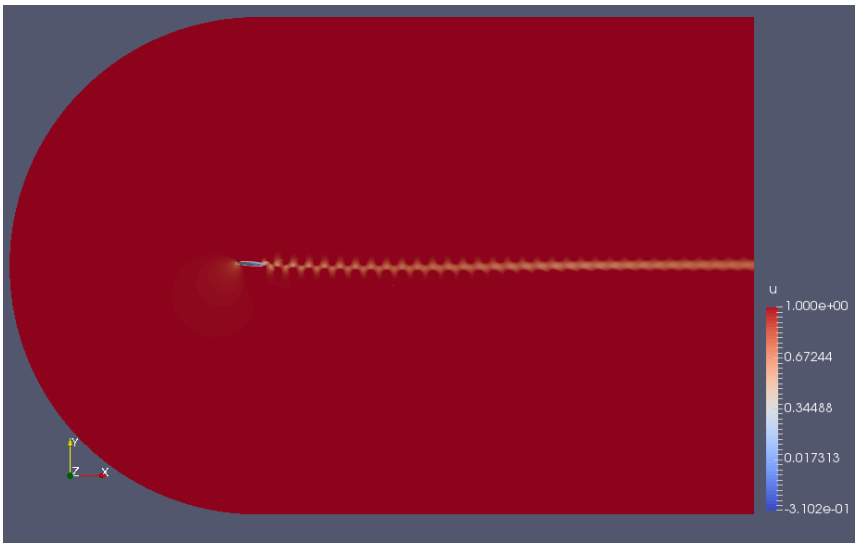

(a) U velocity in all the domain.

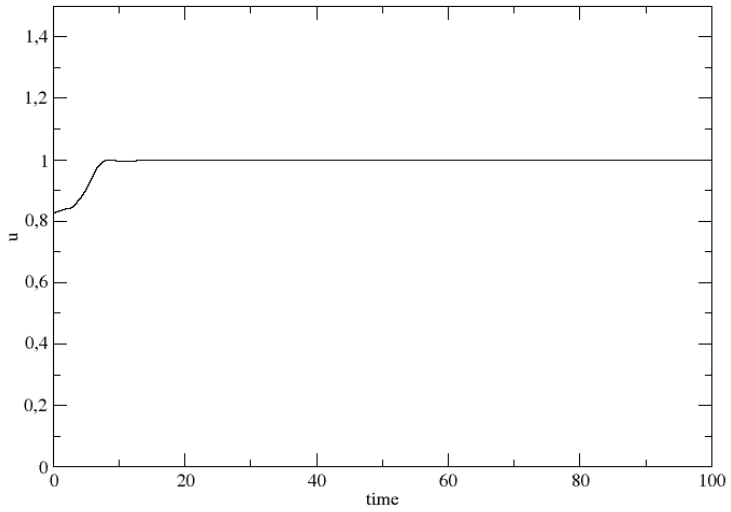

(b) U velocity variation at (-5,0)

Figure C.1: Axial velocity data.

As we can observe from Figure C.1(b) the axial velocity is almost 1 (0.998) and in Figure C.1(a) we can observe the sharp red sorted that is equal to 1 in almost all the domain. This means, that the mesh is good dimensioned to simulate.

C.2. Suction

C.2.1. Streamlines

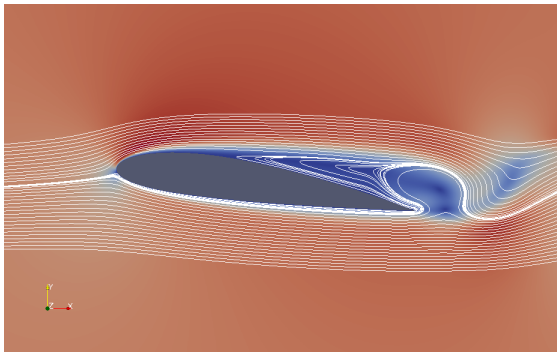

(a) Nominal case.

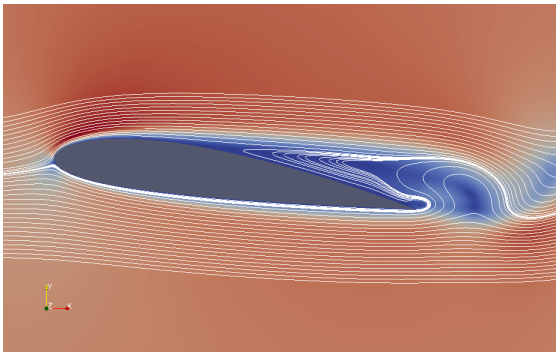

(b) SJA with a 10% suction amplitude.

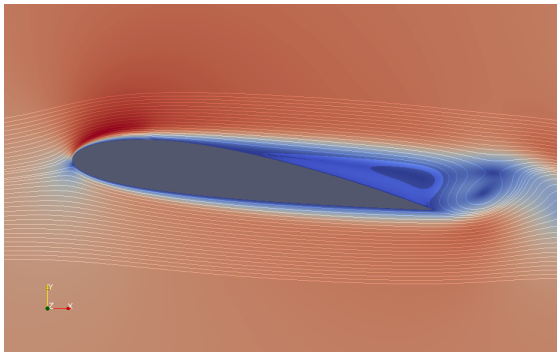

(c) SJA with a 20% suction amplitude.

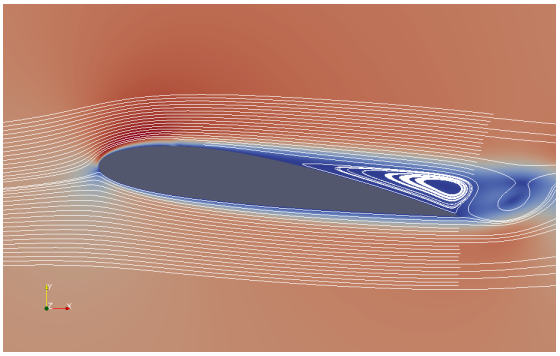

(d) SJA with a 30% suction amplitude.

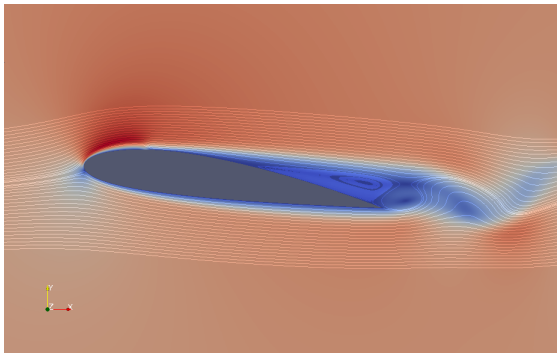

(e) SJA with a 40% suction amplitude.

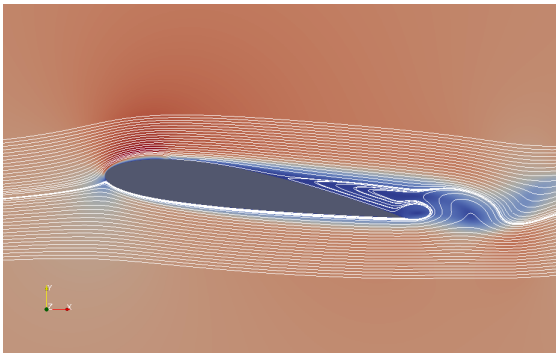

(f) SJA with a 50% suction amplitude.

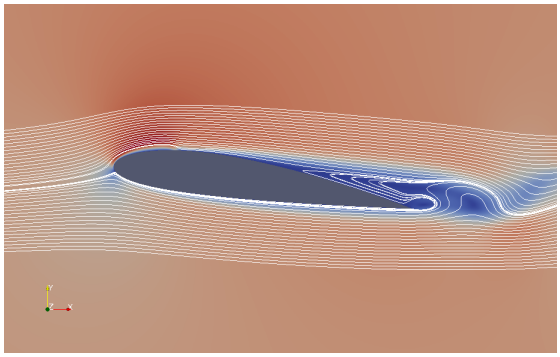

(g) SJA with a 60% suction amplitude.

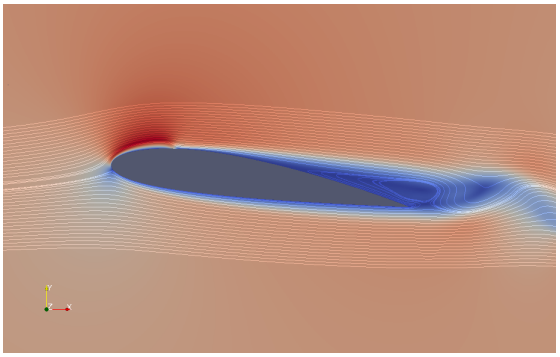

(h) SJA with a 70% suction amplitude.

Figure C.2: Streamlines for different suction amplitudes.

C.2.2. Pressure distribution

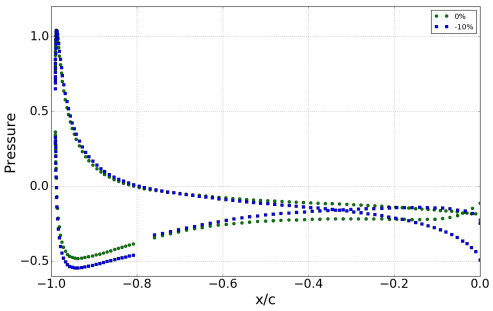

(a) Pressure distribution with a 10% suction amplitude.

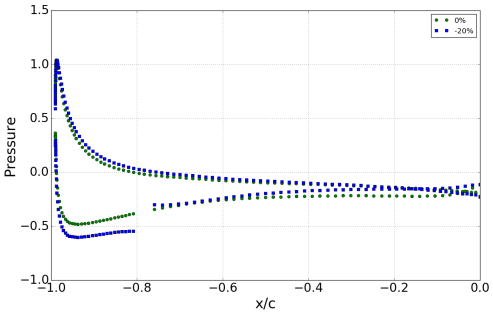

(b) Pressure distribution with a 20% suction amplitude.

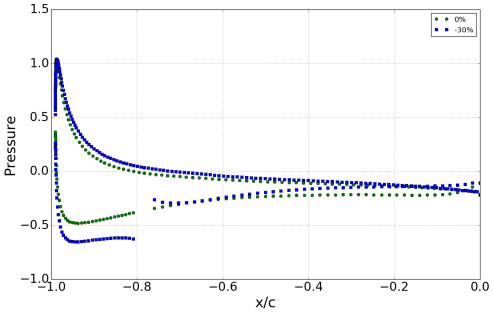

(c) Pressure distribution with a 30% suction amplitude.

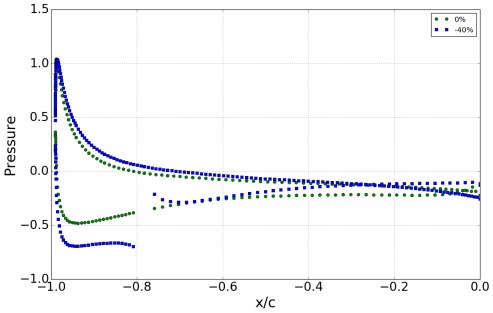

(d) Pressure distribution with a 40% suction amplitude.

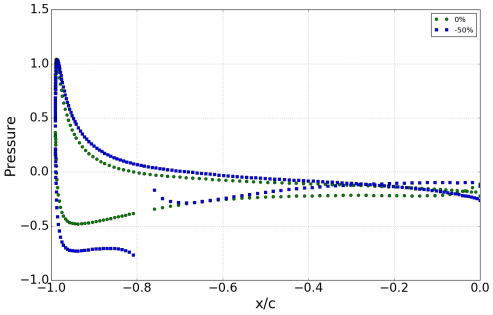

(e) Pressure distribution with a 50% suction amplitude.

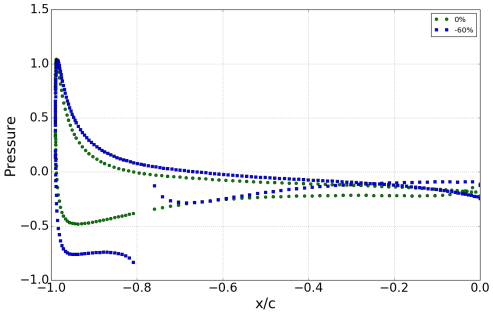

(f) Pressure distribution with a 60% suction amplitude.

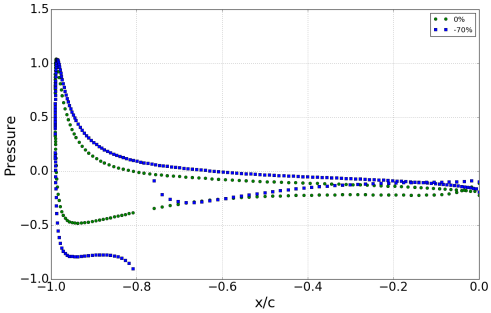

(g) Pressure distribution with a 70% suction amplitude.

Figure C.3: Pressure distribution for different suction amplitudes.

C.2.3. Vorticity

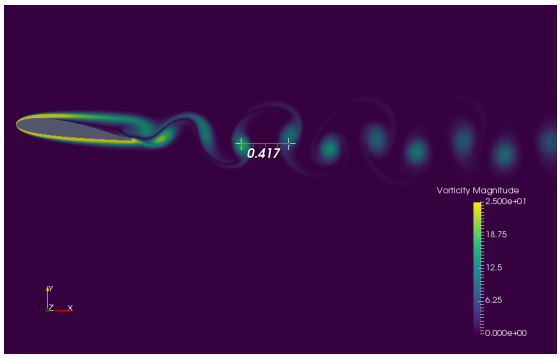

(a) Nominal case.

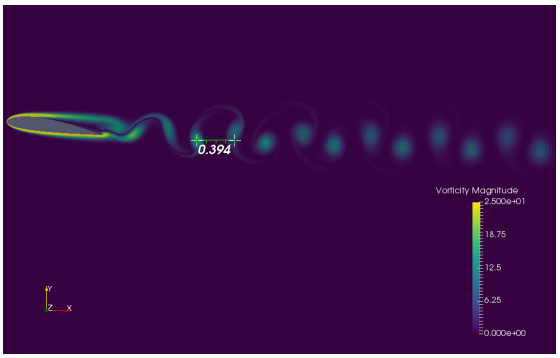

(b) SJA with a 10% suction amplitude.

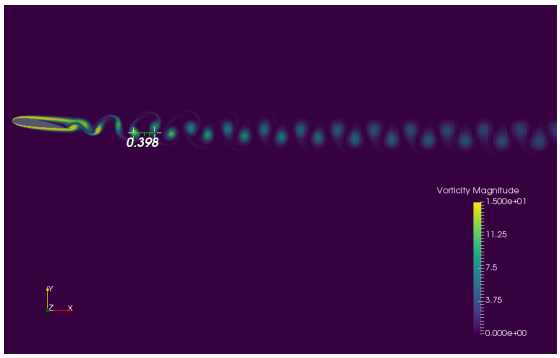

(c) SJA with a 20% suction amplitude.

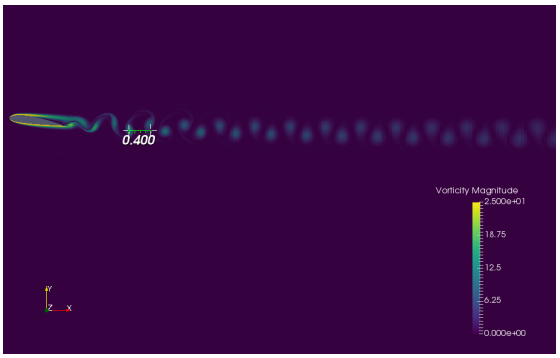

(d) SJA with a 30% suction amplitude.

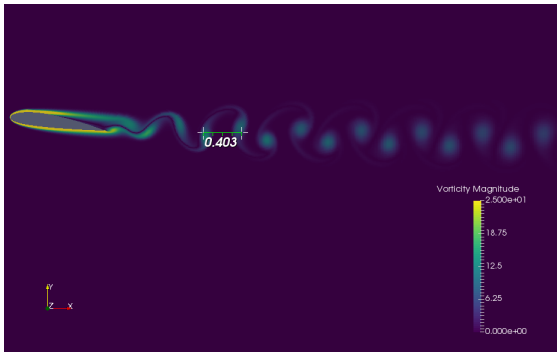

(e) SJA with a 40% suction amplitude.

(f) SJA with a 50% suction amplitude.

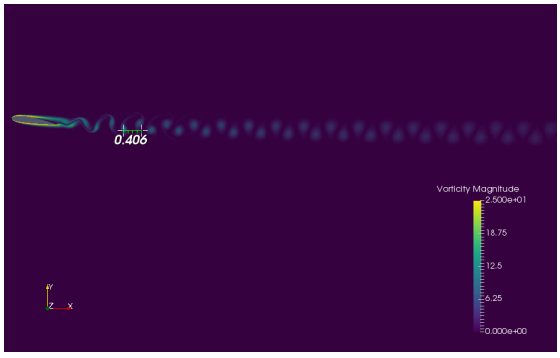

(g) SJA with a 60% suction amplitude.

(h) SJA with a 70% suction amplitude.

Figure C.4: Vorticity for different suction amplitudes.

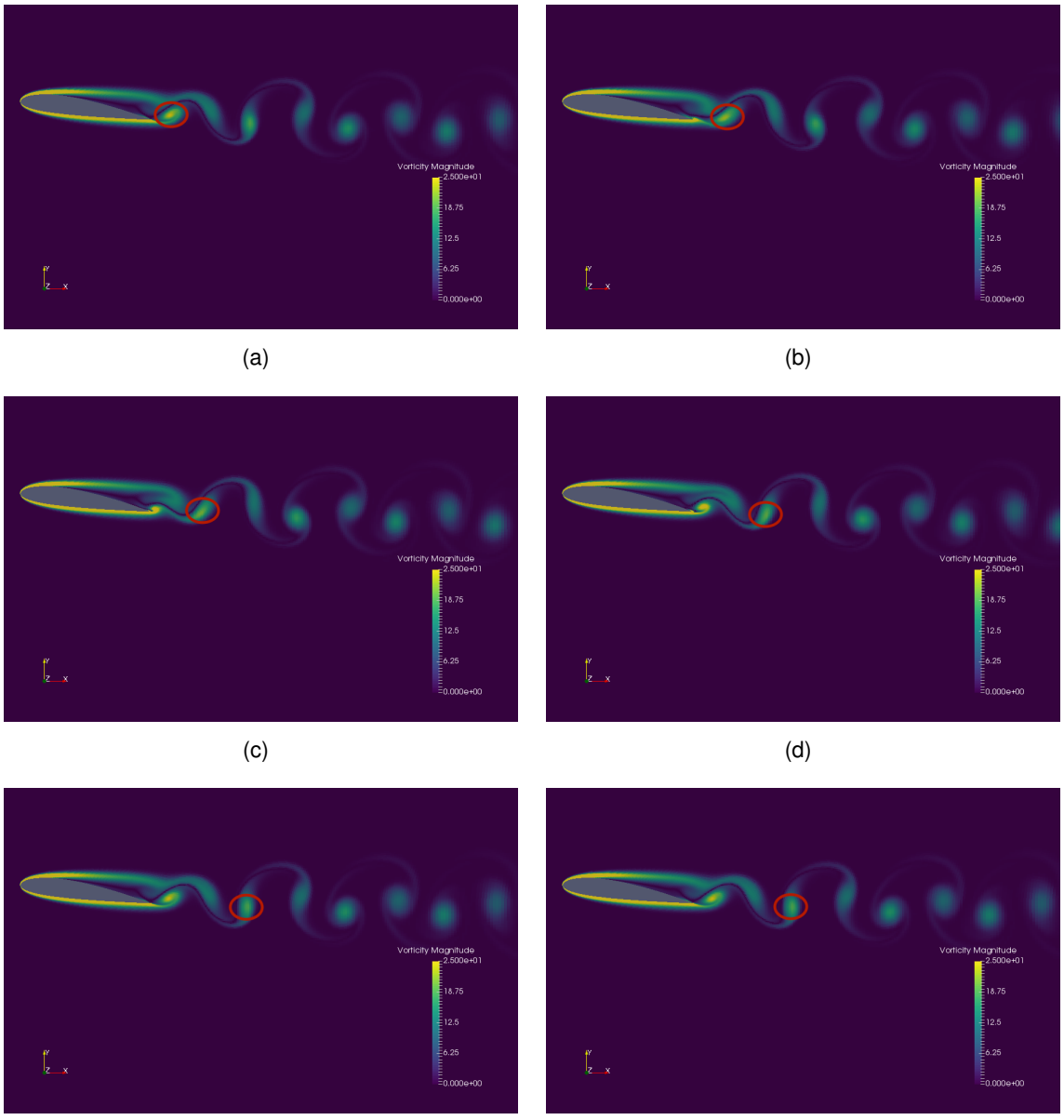

Figure C.5: One cycle vortex shedding at frequency 1.21. The red circle indicates the vortex evolution with time.

C.3. Blowing

C.3.1. Streamlines

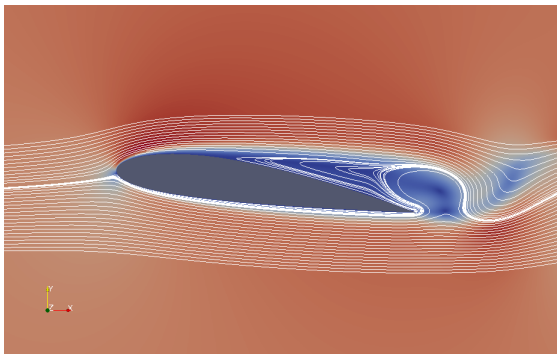

(a) Nominal case.

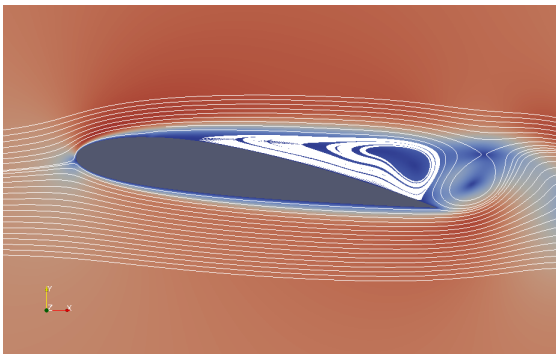

(b) SJA with a 10% suction amplitude.

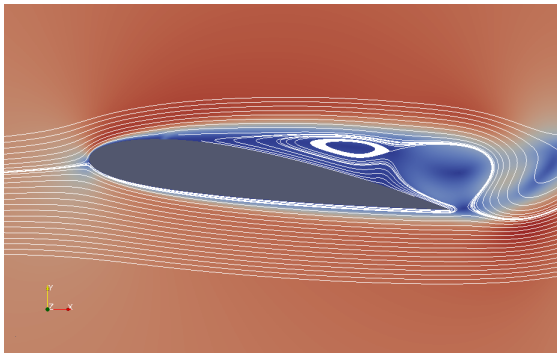

(c) SJA with a 20% suction amplitude.

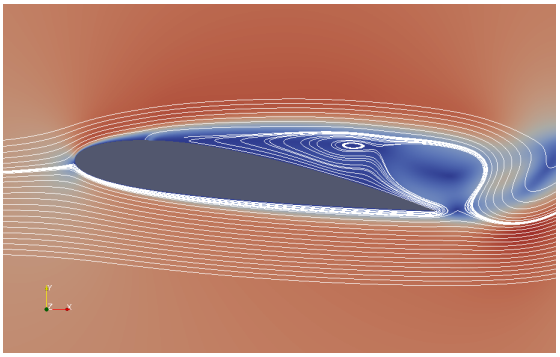

(d) SJA with a 30% suction amplitude.

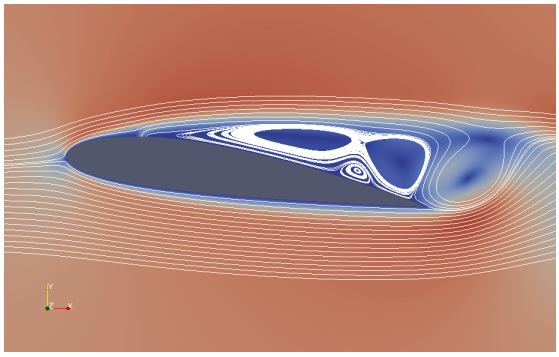

(e) SJA with a 40% suction amplitude.

Figure C.6: Streamlines for different amplitudes.